AU-FREE OHMIC CONTACTS TO GALLIUM NITRIDE AND GRAPHENE

A Thesis

by

PRADHYUMNA RAVIKIRTHI

Submitted to the Office of Graduate and Professional Studies of
Texas A&M University
in partial fulfillment of the requirements for the degree of

MASTER OF SCIENCE

Chair of Committee,	H. Rusty Harris
Committee Members,	Jun Kameoka
	Rupak Mahapatra
	Robert Nevels
Head of Department,	Chanan Singh

August 2014

Major Subject: Electrical Engineering

ABSTRACT

This work deals with Au-free contact metallization schemes for gallium nitride (GaN) and graphene semiconductors. Graphene and gallium nitride are promising materials that can potentially be integrated together in the near future for high frequency high power applications. Realizing and optimizing Au-free technology to GaN and graphene can reduce manufacturing costs and allow the processing of these materials to be compatible with the existing Si-CMOS technology.

For GaN, as a first step, equilibrium energy band diagrams were simulated by solving the Poisson equation in 1-D. Moreover, since tunneling is an important factor in ohmic contacts, tunneling probabilities were simulated for the different potential barriers obtained from solving the Poisson equation. A computationally simple model for calculating contact resistivity as a function of doping concentration and metal work function has been developed. The model was solved numerically to obtain the contact resistivity at each doping concentration and barrier height.

Schottky diodes of TiN and TaN were fabricated and analyzed after rapid thermal anneals (RTA) where performed in the range of 300 ^{o}C to 1100 ^{o}C. J-V characteristics were analyzed extensively both in forward and reverse bias to extract the doping concentration at the metal-GaN interface and the barrier heights. The change in current between different temperature anneals has been attributed primarily due to the change in barrier height and not to the change in doping concentration at the interface.

For graphene, Au-based contacts were fabricated as a baseline and studied at anneal temperatures ranging from 400 ^{o}C to 800 ^{o}C. Experiments with different metallization schemes on graphene proved that stress in the metal films werean important parameter in the realization of Au-free contacts. Stress measurements indicated that Au had a highly compressive contribution to the overall stress in the metal film stack and with this information,Au-free contacts have been engineered using a Al/Ta layer. The Au-free contact scheme was devoid of stress issues and had better ohmic contact parameters than the Au-based contacts.

ACKNOWLEDGEMENTS

I would like to thank my advisor Dr. Rusty Harris for his steady guidance throughout my study under him. I want to express my gratitude to Dr. Derek Johnson for his constant guidance throughout my stay. He helped me learn and master the essential processing techniques required in semiconductor processing. I would also like to thank Dr. Kyoung Lee for providing graphene samples which was essential for my work. Also, I want to thank the other members of Dr. Harris's lab and my committee members.

I would also like to thank my parents for their financial and moral support, without which it would have been impossible for the successful completion of my thesis. I would also like to thank both of my Uncles Mr. Soorya Sharma and Mr. Arvind Sharma for their moral support.

NOMENCLATURE

AlGaN	Aluminum gallium nitride
CVD	Chemical vapor deposition
E_g	Bandgap energy
ε_r	Relative electric permittivity
ε_0	Electric permittivity of vacuum
E_{br}	Break down electric field
GaN	Gallium nitride
HEMT	High electron mobility transistor
J-V	Current density-voltage measurement
μ_n	Mobility of electrons
n_i	Intrinsic electron density
RTA	Rapid thermal anneal
SEM	Scanning electron microscope
Si-CMOS	Silicon complementary metal oxide semiconductor technology
SRH	Schottky-Reed-Hall
TLM	Transfer line method
Θ	Thermal conductivity

TABLE OF CONTENTS

Page

LIST OF FIGURES

LIST OF TABLES

Page

1. INTRODUCTION

1.1.Why gallium nitride and graphene?

The large band gap of gallium nitride, 3.4 eV, allows the material to withstand high breakdown voltages necessary for high power applications. Additionally, it is possible to fabricate AlGaN/GaN heterostructures that exhibit a 2D electron gas, a highly conductive channel with high electron mobility, at the AlGaN/GaN interface. Applications involving high speed and high power require the switching transistors to withstand high electric field during the 'off' state and have minimum conduction losses during the 'on' state. The unique combination of high-electron mobility and high breakdown strength make GaN based heterostructures attractive for such applications [1].

Table 1: Material properties of GaN

	Si	**GaAs**	**GaN**
E_g (eV)	1.1	1.42	**3.39**
μ_n (cm^2/V-s)	1350	8500	**2000 (2DEG)**
E_{br} (MV/cm)	0.3	0.4	**3.3**
Θ (W/cm-K)	1.3	0.43	**1.3**
Hardness (Gpa)	11.5	7	**13.4**
Melting Point (°C)	1414	1238	**2400**

Moreover, as listed in Table 1, GaN has high thermal conductivity, hardness and melting point making it suitable for extreme climate applications. GaN, along with other III-V nitrides, enabled a multi-billion dollar blue, green and white lighting industry [2].

Graphene has extremely unique properties due to its 2D structure, namely, zero bandgap, linear E-k diagram, very high electrical conductivity and most importantly, as shown in Figure 1(c), the ability to invoke its semiconducting properties through the application of a gate voltage [3].

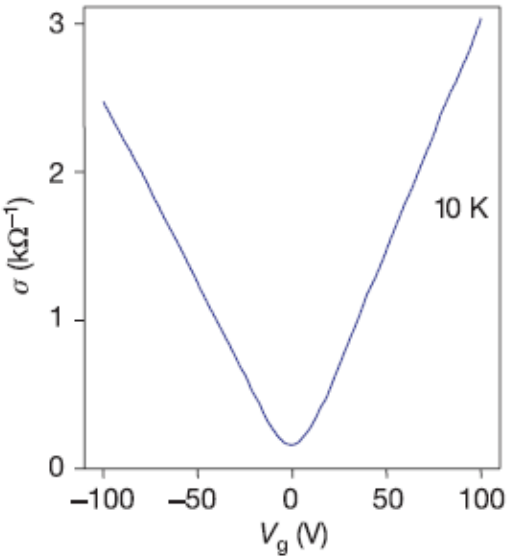

Figure 1: Tunable electrical conductivity of graphene. Reprinted with permission from [4] (Copyright [2005] by Nature Publishing Group)

CVD grown graphene has been developed recently [5], enabling high volume production as well as the ability to transfer graphene to any substrate of interest. Also other methods

of graphene growth have also been achieved in parallel like mechanical exfoliated graphene, epitaxial graphene on SiC and graphene from graphene oxide [6]. Note that CVD grown graphene has the advantage of large area growth and transfer to an arbitrary substrate over the other existing methods. As a result, graphene is receiving significant attention as a potential material for the fabrication of novel electronic devices in the near future.

Application of graphene to transistors is still in its beginning stages. In digital electronics, for a transistor to act as a switch, an important criterion is to have a very low off-state current. However, in graphene, due to its gapless E-k diagram, the off-state current is still high [7]. But in analog electronics, more specifically for ultra-high frequency transistors, graphene is an extremely interesting material which can potentially substitute the current GaAs-based HEMT technology due to the following reasons. First, a relatively small on-off ratio of 10-100 [7] is considered sufficient in analog applications. Hence graphene's gapless spectrum here will not be as a big issue as it is currently in digital electronics. Secondly, the transit time between source to drain is as small as 0.1 ps for a channel length of 100nm, allowing for operating frequencies in the tera-hertz regime.

1.2. Need for a low resistance ohmic contact

A major factor that limits extreme speeds in GaN and graphene based devices is its contact resistance. This is because the cutoff frequency is given by the expression [8],

$$f_T \approx \frac{\mu_{eff}(V_{GS}-V_T)}{2\pi L^2} \tag{1.1}$$

The effective mobility, which physically measures the transit time of an electron from source to drain, gets reduced with higher contact resistance and hence limiting operation in high-frequency applications. For example, Figure 2 shows a graphene based transistor where the transit time of electron from the source to drain of the device is limited due to high contact resistance. The sheet resistance in both graphene and GaN-based HEMT devices is very small and hence it is extremely important to reduce the contact resistance.

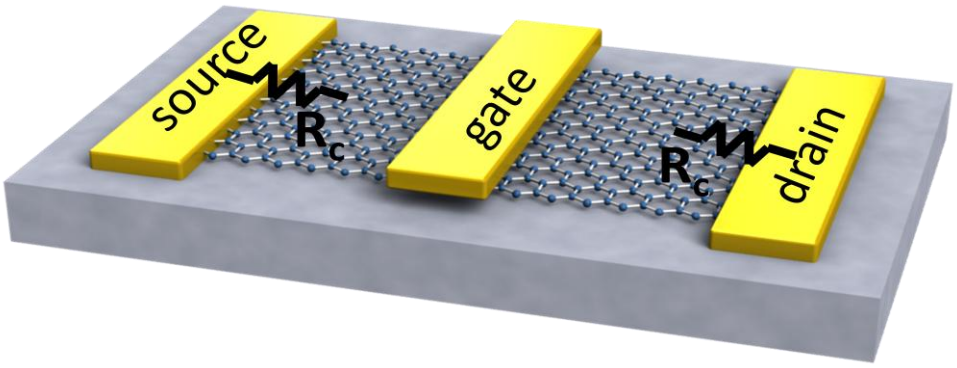

Figure 2 : On current is limited by the contact resistance. Sheet resistance of graphene is very low. Adapted from [9].

Moreover, source and drain contact resistances can cause significant conduction losses especially in high power HEMT devices which operate with high on-currents.

1.3. Why Au-free metallization schemes?

For commercialization of new materials like GaN or graphene it necessary to compete with the existing Si-CMOS technology in terms of cost. Integration of new materials in

the same Si chip to enable cost effective large scale manufacture is on-going. Clearly, for this to happen, the unit processes developed for new materials should be compatible with the existing technology.

Au-free technology is needed to comply with the strict compatibility rules of the Si-CMOS processing lines. Gold has very high diffusivity and can easily diffuse into the active region of a device and destroy its electronic properties by forming mid-band gap traps. Figure 3 shows the energy band diagram of Si and compares to the energy levels of other materials.

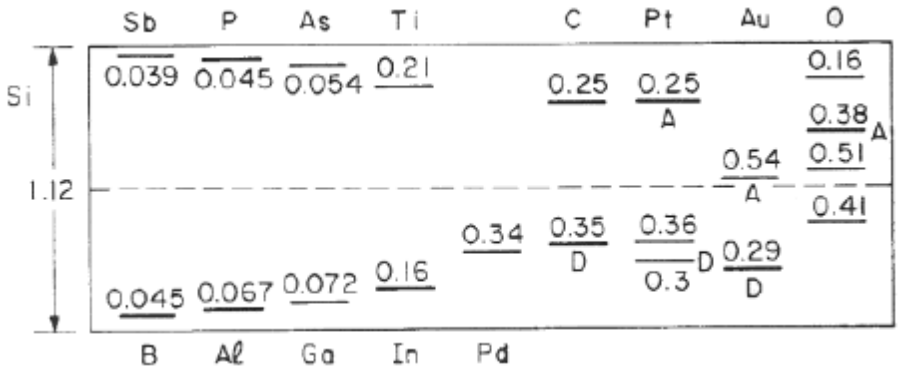

Figure 3: The energy level of Au trap right at the midgap of silicon, acting as an efficient recombination generation site.

It can be observed that trap level of Au is at the midgap of Si. From SRH indirect electron-hole recombination theory, midgap traps are the most efficient recombination centers [10]. Therefore Au contamination in silicon can reduce the carrier lifetimes in silicon, hindering normal device performance.

Another advantage of using Au-free metallization schemes is that the cost of production is reduced by avoiding expensive gold.

1.4. Importance and focus of the present work

Ohmic contact metallization schemes in literature has either Ti or Ta as the interface material. It is believed that Ti and Ta, both form a thin interfacial nitride enabling ohmic contact formation [11]. The focus of this work on GaN is twofold. Firstly, to understand the ohmic contact formation better by fabricating TiN and TaN diodes and extracting the barrier height at different anneal temperatures. Secondly, to fabricate better Au-free contacts by co-sputtering two materials of interest, like Ti and Ta, and determining the optimum alloy composition that would give the least contact resistance.

For Graphene, there are several Au-based contacts reported in literature [12-14]. These contacts make use of a Ti, Ni, Pd or combination of these materials as the first layer, followed by a thick Au capping layer. Au-free contacts have not been reported in literature for CVD grown graphene. The purpose of the work is to understand the importance of Au in these contacts and effectively replace Au with Au-free contacts.

It is possible to make devices using both GaN and graphene, which would require Au-free metallization schemes. This is due to a few reasons the first of which is the ability to form a 2DEG channel using GaN-based hetero-structure with a very high electron mobility. Graphene also has high electron mobility due to its 2-D structure, therefore it will be interesting to make a device for high speed high power applications which utilizes the high electron mobility of GaN and graphene. GaN and graphene have

hexagonal lattice geometry making the transfer of graphene on to gallium nitride possible and the fabrication of such a future device more practical.

1.5. Organization of the report

The second chapter focuses on the general understanding of ohmic contacts to gallium nitride through simple quantum mechanical models. First, the energy band diagram at equilibrium is simulated for various metal work functions and semiconductor doping concentrations. The tunneling probability is computed for the barriers obtained from solving the Poisson's equation. A computationally simple mathematical model for calculating the contact resistivity is formulated which makes use of the calculated tunneling probability. Finally, the contact resistance is simulated for different doping concentrations and metal work functions.

The third chapter focuses on ohmic contacts to gallium nitride. First, the J-V characteristics of TiN and TaN schottky diodes are studied in forward and reverse bias to obtain the barrier heights at different doping concentrations. Second, the contact resistances for co-sputtered Ta and Ti contacts are studied at different anneal temperatures and compared to the baseline.

The fourth chapter focuses on Au-free contacts to graphene. As a first step, the challenges of obtaining Au-free contacts are explored through trial error of various Au-free schemes. Next, the role of Au in the stress of the metal stacks of interest is investigated through Flexus measurements. Once the role of Au was well understood, Au-free contacts were designed. The designed Au-free contacts were characterized fully

at different anneal temperatures and compared to the Au-based baseline and literature. The final chapter summarizes the findings in chapter 2-4 and discusses future research that can stem out of the present work.

2. UNDERSTANDING OHMIC CONTACTS TO GAN VIA SIMULATIONS

2.1. Equilibrium energy band diagram

When a metal is in contact to a semiconductor, the electric potential at every point can be obtained by solving the Poisson equation, given in 1-D by

$$\frac{d^2V}{dx^2} = -\frac{q\left(-n(x)+N_D^+\right)}{\epsilon_0\epsilon_r} \tag{2. 1}$$

Where n(x) and N_D^+ denote the electron and donor concentration of the semiconductor respectively. Making use of depletion approximation, the above expression can be simplified as

$$\frac{d^2V}{dx^2} = -\frac{qN_D^+}{\epsilon_0\epsilon_r} \tag{2. 2}$$

The boundary conditions for the above expression is given by

$$V(0) = \phi_M - \phi_s; V(W_b) = 0 \; and \; E(W_b) = 0 \tag{2. 3}$$

where $\phi_M, \phi_s, W_b, V \; and \; E$ are the metal work function (W.F), semiconductor work function, depletion width, electric potential and electric field respectively.

The solution was plotted for different doping concentrations and metal work functions as shown in Figure 4. For ohmic contacts, a low barrier height and a small barrier width is preferred. This is obtained when the doping in the semiconductor right at the interface is high and the W.F of the metal is as close to the conduction band edge. Hence, as the simulation results indicate, a high doping leads to a thinner barrier and if the W.F of the metal is close to the conduction band edge, a shorter barrier will be realized.

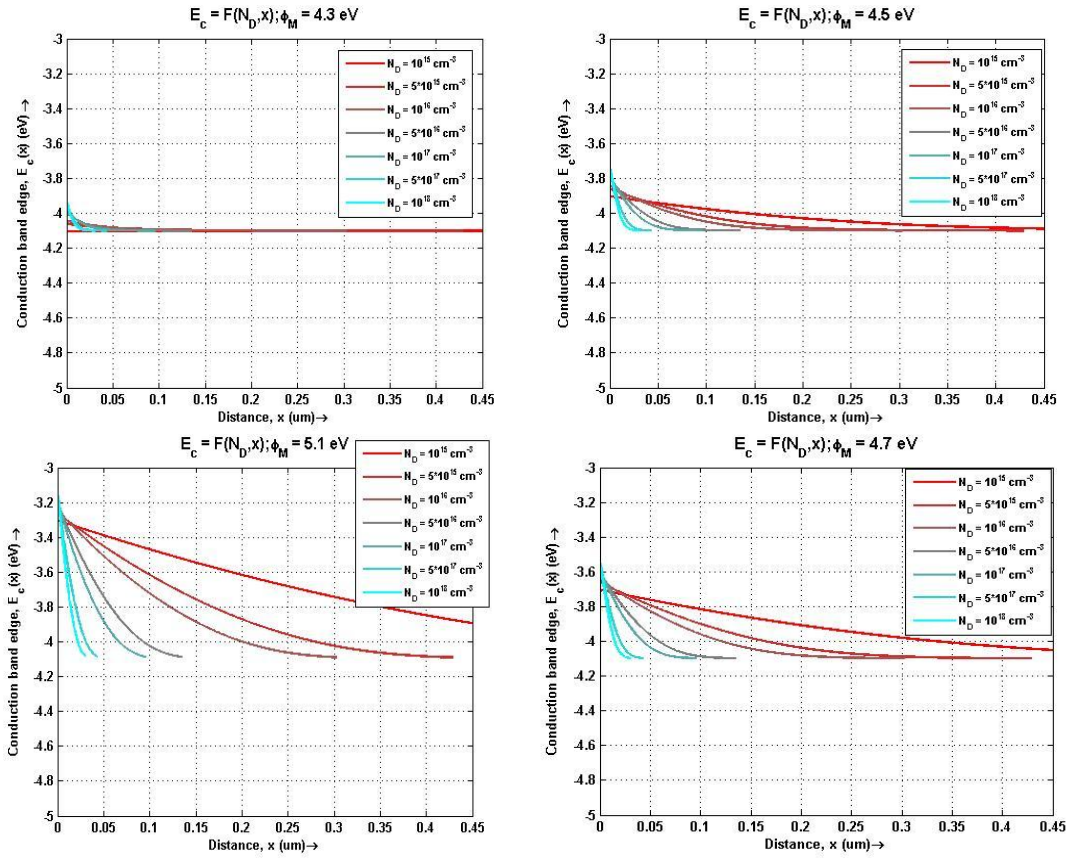

Figure 4: Simulation results obtained via depletion approximation that show conduction band edge for GaN in equilibrium with metals of different W.F.

The depletion approximation, which was used to obtain the simulations shown in Figure 4 cannot be used in case the metal work function goes below the Fermi-level of GaN. In this case, eqn (2.1) has to be solved numerically to obtain the energy band diagram at equilibrium. The procedure is discussed in detail in Appendix A. Figure 5 shows the conduction band edge of GaN at equilibrium with metals of various work functions, obtained through the numerical simulation of Poisson equation. It should be noted that the depletion approximation, in Figure 4, can be used when the metal W.F is larger than

the electron affinity of GaN which agrees well with the simulation results obtained via numerical simulation. However, it is impossible to analytically solve the Poisson equation (through the depletion approximation) when the work function of the metal is lower than the work function of the semiconductor.

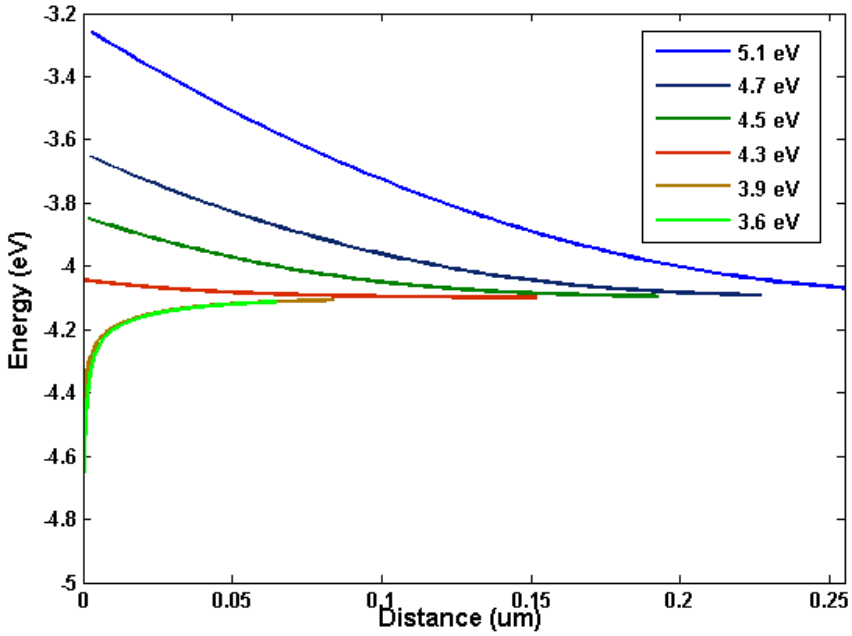

Figure 5: Conduction band edge of GaN at equilibrium at a fixed doping concentration in contact with metal of different W.Fs obtained through numerical simulations of the Poisson equation.

2.2. Electron tunneling probability through a barrier

The current through a barrier occurs through separate mechanisms

(i) Thermionic emission over the barrier

(ii) Tunneling through the barrier

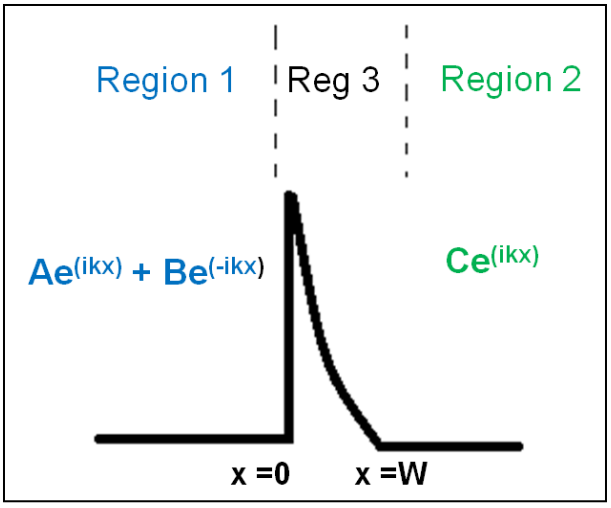

Figure 6: Schematic illustrating the procedure for solving Schrödinger equation

For ohmic contacts tunneling through a potential barrier becomes significant. To solve for the tunneling probability through a barrier it is necessary to solve the Schrödinger equation under the appropriate boundary conditions. For the barrier as shown in Figure 6, Schrödinger equation is given by

$$-\frac{\hbar^2}{2m^*}\frac{d^2\psi}{dx^2} + V(x)\psi = E\,\psi \qquad (2.4)$$

Where E is the total energy of the electron incident from the left of the barrier and V(x) is potential of the barrier. The above Schrödinger equation solved analytically in regions I and III is given by the expression below:

$$\psi_I = Ae^{ikx} + B\,e^{-ikx} \qquad (2.5)$$

$$\psi_{III} = D\,e^{ikx} \qquad (2.6)$$

where $= \sqrt{\frac{2m^*E}{\hbar^2}}$; A,B and D are complex coefficients. However, the Schrödinger equation has to be solved numerically in the region II. Note that the potential V(x) is already obtained from the solution of Poisson's equation discussed in section 2.1. The constants A, B and D can be related to one another using the following boundary conditions

$$\psi(x = 0^-) = \psi(x = 0^+) \tag{2. 7}$$

$$\psi(x = L^-) = \psi(x = L^+) \tag{2. 8}$$

$$\frac{d\psi}{dx}(x = 0^-,) = \frac{d\psi}{dx}(x = 0^+) \tag{2. 9}$$

$$\frac{d\psi}{dx}(x = L^-) = \frac{d\psi}{dx}(x = L^+) \tag{2. 10}$$

The tunneling probability can be determined by the expression

$$T(E) = \left|\frac{D}{A}\right|^2 \tag{2. 11}$$

Figure 7 shows the simulated transmission coefficient at a fixed doping for different metal work functions. The dotted lines in the figure correspond to the top of barrier with respect to the vacuum level. Notice that the there is significant transmission through the barrier when the doping concentration becomes larger, coherent with the fact that it is easy to tunnel through a thinner barrier.

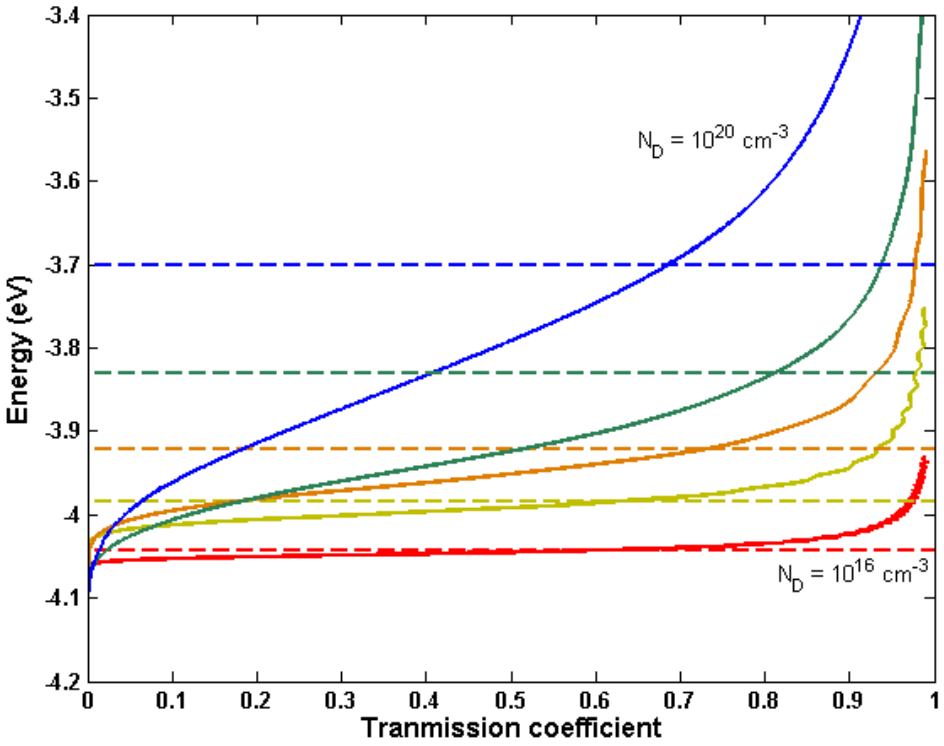

Figure 7: The transmission through a barrier at different doping concentrations at fixed metal work function of 4.5 eV. The dotted lines represent the top of the barrier at each doping concentration

2.3. Formulation of specific contact resistance model

Now that the Poisson equation has been solved and transmission at equilibrium has been obtained, it is possible to compute the contact resistivity for all doping concentrations and metal work functions. The current density through an arbitrary barrier can be related to transmission through the barrier by the following relationship [15] :

$$J = \frac{2q}{(2\pi)^3} \iiint d^3k \, v_z(k_z) T(E_z)[F_s - F_m] \qquad (2.12)$$

where $F_s \, and \, F_m$ are the Fermi-level occupation probabilities at the metal and semiconductor respectively given by

$$F_s = \frac{1}{1+\exp\left(\frac{E_{f0}+E}{k_bT}\right)} \quad (2.13)$$

$$F_m = \frac{1}{1+\exp\left(\frac{E_{f0}+E+qV}{k_bT}\right)} \quad (2.14)$$

Where V is the applied voltage and E_{f0} is the Fermi level at equilibrium . The various terms in Eqn (2.12) can be simplified using Taylor series as follows

$$F_s - F_m = \left(-\frac{dF_s}{dE}\right) qV + (higher\ order\ V) \quad (2.15)$$

$$v_z = \frac{1}{\hbar}\frac{dE_z}{dk_z} \quad (2.16)$$

$$T(E_z, V) = T(E_z, 0) + \left(\frac{dT}{dV}\right)|_{V=0} V + (higher\ order\ V) \quad (2.17)$$

Collecting first order

$$J = \frac{2q}{(2\pi)^3}\ (qV) \iiint d^3k\ v_z(k_z) T(E_z, 0) \left(-\frac{dF_s}{dE}\right) + (higher\ order\ V) \quad (2.18)$$

$$J = \left(\frac{1}{\hbar}\right)\frac{2q}{(2\pi)^3}\ (qV) \int_0^\infty dE_z T(E_z, 0) \iint d^2k_\perp \left(-\frac{dF_s}{dE}\right) + (higher\ order\ V) \quad (2.19)$$

Now consider,

$$I_1 = \iint d^2k_\perp \left(-\frac{dF_s}{dE}\right) \quad (2.20)$$

Eqn (2.20) can be simplified further by changing the variable of integration from k space to v space using the substitution,

$$dk_x = \left(\frac{m^*}{\hbar}\right) dv_x; dk_y = \left(\frac{m^*}{\hbar}\right) dv_y \quad (2.21)$$

Also making note of the fact that

$$E = E_z + \frac{1}{2}m^* v_x^2 + \frac{1}{2}m^* v_y^2 \quad (2.22)$$

The variable of integration can be changed from x-y space to r-θ space as follows

$$dk_x dk_y = \left(\frac{m^*}{\hbar}\right)^2 dv_x dv_y = \left(\frac{m^*}{\hbar}\right)^2 v_r dv_r dv_\theta \quad (2.\ 23)$$

Where

$$v_r = v_x^2 + v_y^2 \; and \; v_\theta = \text{atan}\left(\frac{v_y}{v_x}\right) \quad (2.\ 24)$$

Making use of the above substitutions and simplifying, eqn (2.20) becomes

$$I_1 = \frac{2\pi m^*}{\hbar^2} F_s(E_z) \quad (2.\ 25)$$

Substituting in eqn (2.19) we obtain,

$$J = \frac{4\pi q^2 m^*}{h^3}(V) \int_0^\infty dE_z F_s(E_z) T(E_z, 0) \; + (higher \; order \; V) \quad (2.\ 26)$$

The specific contact resistivity is defined as the inverse of the slope of J-V characteristics at V=0. Mathematically,

$$Rc = \left(\frac{\partial J}{\partial V}|_{V=0}\right)^{-1} = \frac{1}{\left(\frac{A^* q}{k_b^2}\right) \int_0^\infty dE_z T(E_z) F_S(E_z)} \quad (2.\ 27)$$

Note that the higher order voltage terms vanish when we set V=0. Also, the constant A* is called the Richardson constant, defined as

$$A^* = \frac{4\pi q m^* k_b^2}{h^3} \quad (2.\ 28)$$

The method for computing eqn (2.27) for contact resistivity is listed in steps as below:

(i) Solve for the Fermi-level at equilibrium based on the doping concentration of the semiconductor

(ii) Solve the Poisson equation for a given metal work function to obtain the electric potential V(x) as discussed in section 2.1

(iii) Solve for transmission through the potential V(x) as discussed in section 2.2.

(iv) Plug the numerically obtained expression for transmission in eqn (2.11) to obtain contact resistance for every value of doping and metal work function.

Section 2.4 analyzes the results obtained through the above procedure. Eqn (2.27) is a very useful tool to compute contact resistivity for the following reasons

(i) The expression only requires the transmission through a barrier and Fermi-level distribution at equilibrium. Hence it is not necessary to simulate energy band diagrams at non-equilibrium.

(ii) The derivation of the expression is very general. It does not make use any of the common assumptions made in semiconductor physics like Boltzmann approximation, depletion region approximation or W.K.B approximation. Moreover, the expression accounts for both thermionic emission and tunneling.

(iii) Computationally, the integration that has to be performed is straightforward and does not require tedious iterations once the transmission through a barrier is computed.

2.4. Simulation of contact resistivity at different doping and barrier heights

The contact resistivity was computed for different doping and metal work functions for GaN as discussed in section 2.3. Figure 8 shows the contact resistivity as a function of metal work functions to GaN for various doping concentrations, whereas Figure 9 shows the contact resistivity as a function of doping concentration.

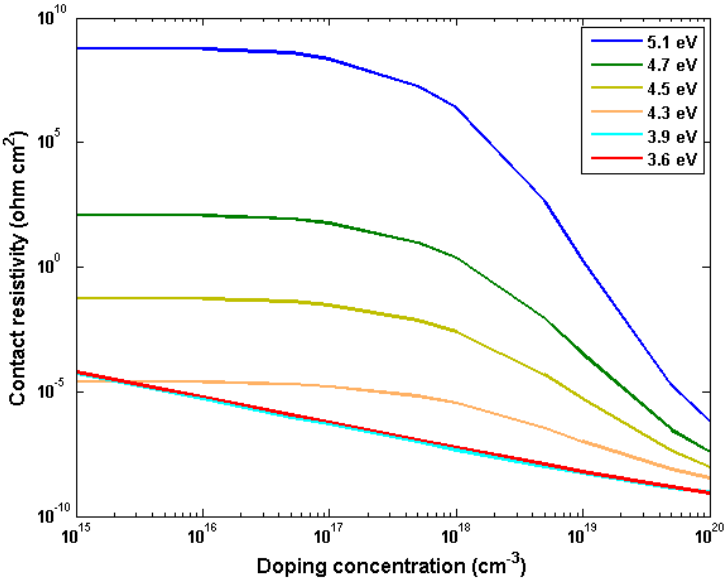

Figure 8: Contact resistivity as a function of doping for different metal W.Fs

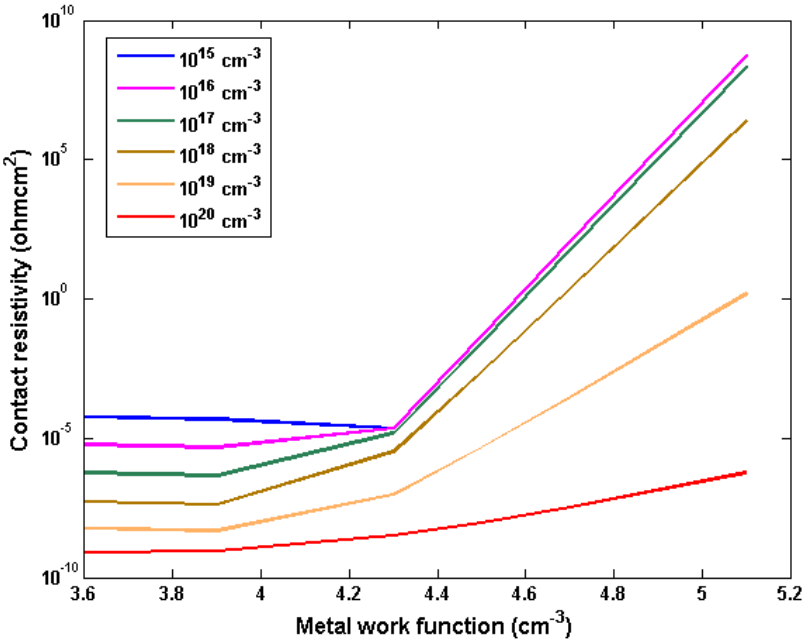

Figure 9: Contact resistivity as a function of W.F for different doping concentrations

For doping concentrations in the range of 10^{15} to 10^{18}, it is clear that a change in barrier height (metal W.F) has a greater effect on contact resistivity than the change in doping concentrations itself. However, when doping concentrations becomes greater than 10^{18} (degenerate GaN at the interface), there is a strong dependence of contact resistivity on both doping and barrier height. Also, if it possible to achieve complete control over barrier height and interface doping, it is possible to achieve contact resistivity of around 10^{-9} Ωcm^2. The baseline contact to GaN (will be established in section 3) is around 10^{-5} Ωcm^2 which suggests there is potential for improvement.

Simulations suggest that , we can change the contact resistivity by orders of magnitude if it possible to tune the interface doping concentration or metal work function. As explained in section 3, interface doping concentration can be changed by using a metal that can form a thin metal nitride at the interface and metal work function can be tuned by the use of a co-sputtered contact.

3. AU-FREE SCHEME FOR GALLIUM NITRIDE

3.1. Survey of Au-free contacts in literature and scope for improvement

For n-type GaN, it was observed that aluminium and gold form poor ohmic contacts (resistances in the order of 10^{-3} Ω/cm^2) to GaN [16]. As-deposited Al showed ohmic behaviour, but as-deposited Au showed rectifying behaviour. Au contact became ohmic after annealing at 575 ^oC. However, literature proves that multi-layered metals form better ohmic contacts. Kahn et al [17] used a Ti/Au bilayer and found specific resistance to be 8×10^{-5} Ω/cm^2 before annealing and 8×10^{-6} Ω/cm^2 after RTA at 900 ^oC for 30 s. Similarly Ti/Ag ohmic contact showed specific resistance of 6.5×10^{-5} Ω/cm^2 before annealing [18]. Lin et al [19] used Ti/Al and found better results for ohmic resistance compared to GaN[17]. However, Ti/Al contacts lost its stability at high temperatures due to formation of aluminium lumps on the surface, increasing its roughness and resistance. Fan et al [20] achieved an ohmic resistance of around 10^{-7} Ω/cm^2 for a n-type doping of 2×10^{17} cm^{-3} using a composite metal layer of Ti/Al/Ni/Au (150 Å/2200 Å/400 Å/500 Å).RTA was done at 900 ^oC for 30s. The formation of TiAl and conductive TiN is believed to be the reason for low resistance ohmic contacts. The Al layer is 2000 Å thick which prevents the out diffusion of Ga andallows for a certain amount of Au and Ni interdiffusion that forms a TiAl/AuNi phase in contact with GaN. This supports the idea that TiN plays a pivotal role in ohmic behaviour.

For AlGaN/GaN HEMTs Au-free technology has been realized recently [1, 21-23], but there is still room for optimization of contact resistance and uniformity. Two primary metallization schemes are being explored for ohmic contact: Ti-based [1, 21, 22] and Ta-

based [24, 25]. Similar to studies in n-GaN, it is believed that N from GaN out diffuses to form a thin interfacial layer of TiN or TaN at the metal-GaN interface during the ohmic contact formation. This effectively dopes the GaN to a high value, reducing the barrier width and increasing the tunneling current.

Therefore, two factors dictate ohmic behaviour. Firstly, it is necessary to form an interfacial nitride at the interface of gallium nitride and the deposited metal. This interface layer reduces the barrier width. Secondly, the effective work function of the metal stack-metal nitride composite should be as close to the conduction band edge of GaN as possible. This will decrease the barrier height. As shown in chapter 2, the contact resistance will be a minimum when it is possible to achieve a reduction in barrier height as well as barrier width.

Since Ti and Ta have been the interface metal of choice for ohmic contacts in literature, it is crucial to understand the electrical properties of the corresponding metal-nitride (TiN or TaN) that is formed at the interface. Hence the first step would be to study the electrical properties of TiN and TaN metal-GaN junctions. As discussed earlier, the out diffusion of N from GaN is crucial in achieving ohmic behaviour to gallium nitride. . Figure 10 shows a energy band diagram schematic of junction with and without N out diffusion. Hence it is expected that TiN or TaN contacts would be rectifying in nature, as they will not allow much N out diffusion as deposited or after annealing.

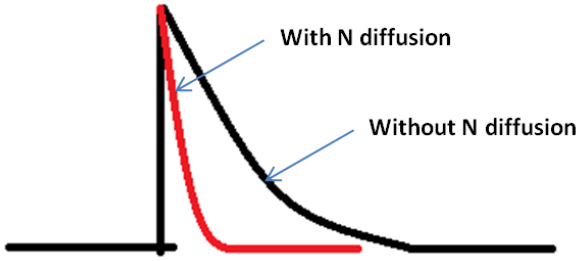

Figure 10: Energy band diagram schematic for a contact with and without N-diffusion

By studying the electrical properties of TiN and TaN schottky diodes it is possible to extract the barrier height. Also the contacts employed in literature anneal their contacts from a range of 600 ^{o}C to 900 ^{o}C. Hence it is also important to study the effect of barrier height on annealing at different temperatures. Section 3.2 of this chapter discusses the fabrication and analysis of TiN and TaN schottky contacts to gallium nitride, as-deposited and annealed in the range 300 ^{o}C-1100 ^{o}C.

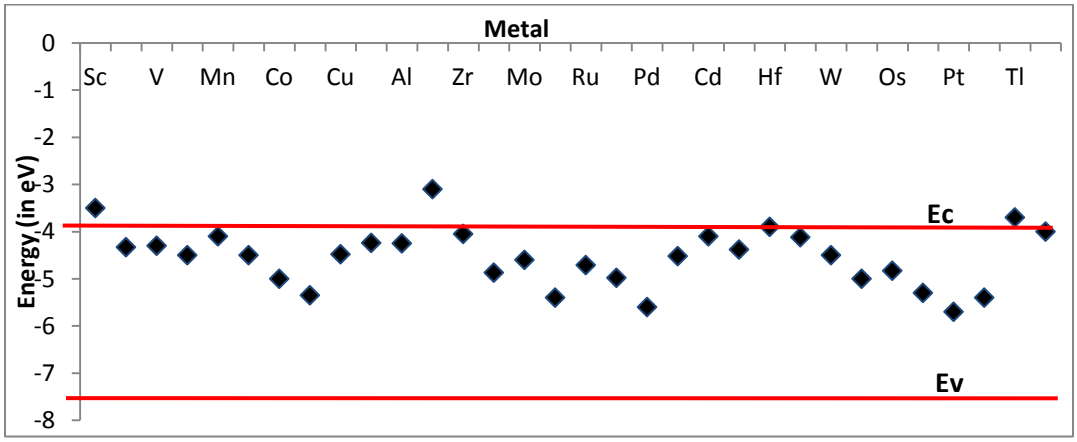

Figure 11: Work function of the various metals in the periodic table and compared to the conduction band edge of gallium nitride.

The next step is to engineer the work function of the metal to allow for a low barrier height, which is favorable for an ohmic contact. Figure 11 shows the work function of all the metals in the periodic table compared against the conduction band edge of gallium nitride [26, 27].

Of these metals, only a few of the metals can form a metal nitride. In other words, only some of the metals have a negative enthalpy of formation. Figure 12 shows a plot of work function versus formation enthalpy of the corresponding nitride [28].

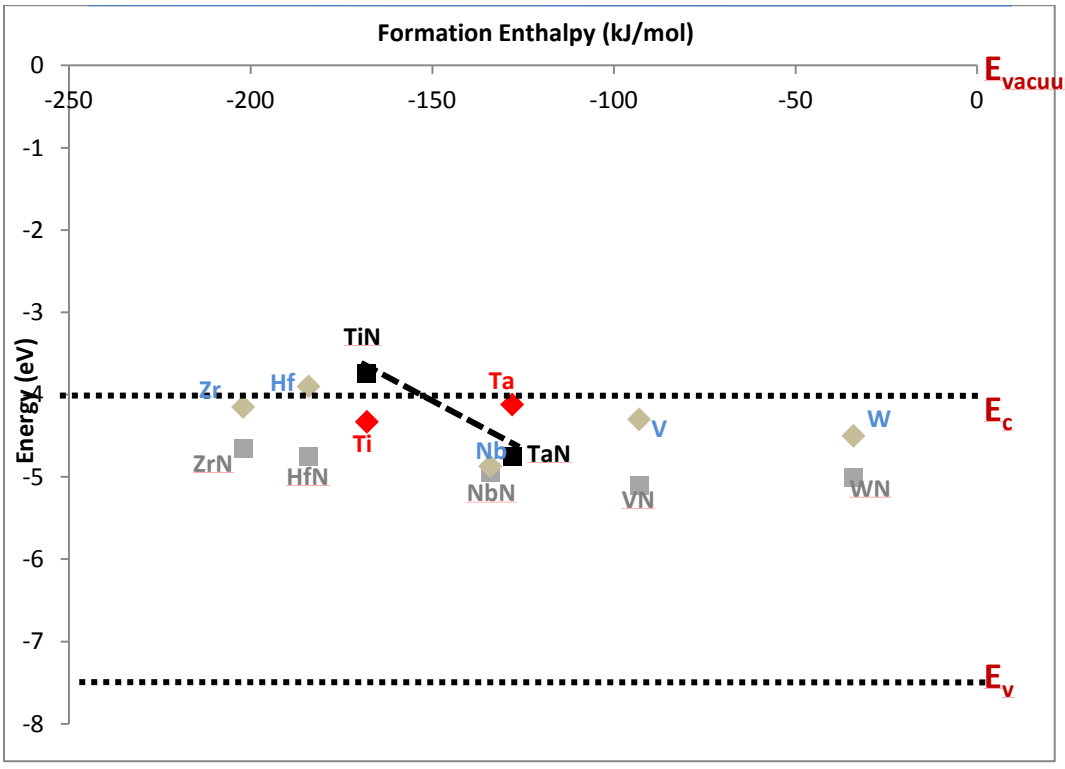

Figure 12: W.Fs of metals plotted against their corresponding nitride formation enthalpy. The dotted lines connecting TiN and TaN is a first order approximation to the work function of a ternary nitride achieved by varying the Ti and Ta compositions.

Figure 12 also highlights the work functions of Ti and Ta along with its corresponding nitride. The dotted line connecting the TiN and TaN is the expected work function (first order of approximation) of the metal that would be formed at the GaN interface..Therefore, Ti and Ta can be co-sputtered at different compositions to achieve $Ta_xTi_{1-x}N$, a ternary metal nitride at the GaN interface. The work function of $Ta_xTi_{1-x}N$ can be given approximately to the first order by the following expression

$$WF_{Ti_xTa_{1-x}N} = WF_{TaN}.(x) + WF_{TiN}\,(1-x) \qquad (3.1)$$

Now, by varying the composition 'x' in the above expression, it will be possible change the work function of the metal nitride to match the conduction band edge of gallium nitride. Section 3.3 of this chapter discusses the fabrication procedure and analysis for the co-sputtered Ti_xTa_{1-x} contacts.

3.2. Process steps: TiN and TaN schottky diodes

This section explores the fabrication and electrical characterization of TiN and TaN schottky diodes. As discussed in section 3.1, the purpose of characterizing TiN and TaN diodes is to extract the barrier height information and hence help better understand the mechanism for ohmic contact formation in GaN.

The process steps in the fabrication of TiN and TaN schottky diodes are as shown in Figure 13.

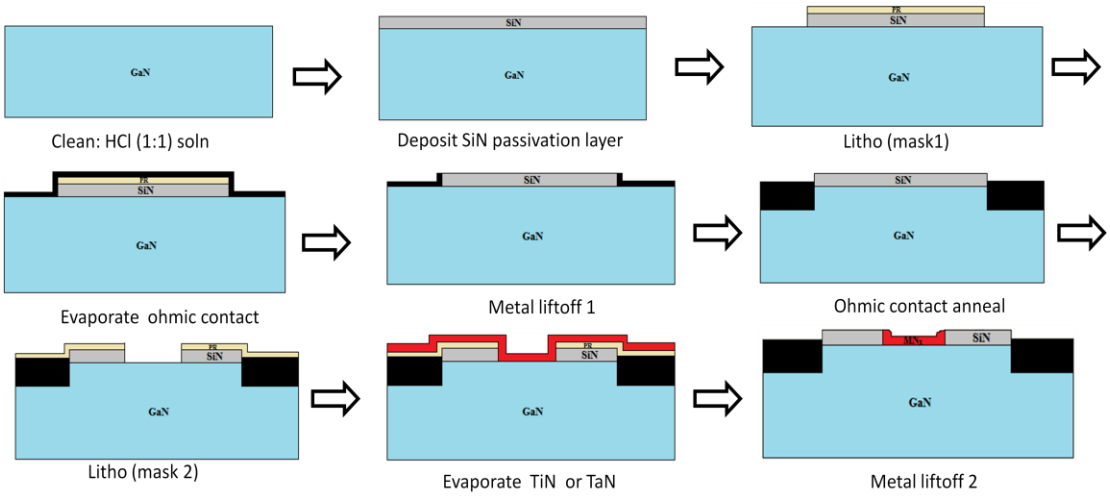

Figure 13: Process steps in the fabrication of TiN and TaN diodes

Clearly, the fabrication steps can be split into two major steps:

(i) Fabricating ohmic contacts of known contact resistance to GaN

(ii) Fabrication of TaN or TiN schottky contacts.

3.2.1. Obtaining an ohmic contact baseline to gallium nitride

The first step necessitates the fabrication of a known ohmic contact. TLM structures (discussed in Appendix B), were fabricated through a liftoff process. An enclosed TLM structure was used with TLM spacing ranging from 9 um to 55 um. An enclosed structure, unlike a linear one, has the advantage of not using any device isolation (like mesa or ion-implantation isolation), saving one photo lithography step. However, a correction factor has to be used to compensate for geometry of the enclosed structure [29].

Au-based and Au-free metal stacks were used to obtain the baseline contact to gallium nitride. Ti/Al/Ni/Au (30/180/40/50 nm) was used as the Au-based baseline. Ti/Al/Ni was evaporated in an e-beam and Au was deposited via DC sputtering. Ohmic behaviour was enhanced after a 900 ^{o}C, 30sec RTA in N_2 ambience. Ta/Al/Ta (100/2800/20 nm) [25] evaporated via e-beam was used as the Au-free baseline. Ohmic contact was established after a RTA at 575C, 4min in N_2 ambience.

The contact resistance was extracted by extrapolating the linear curve to L=0 and dividing the result by 2. (TLM fundamentals can be found in Appendix B). The specific contact resistivity was calculated using eqn (B2). Figure 14 shows the TLM plot and Table 2 shows the important parameters that can be extracted from the TLM measurement.

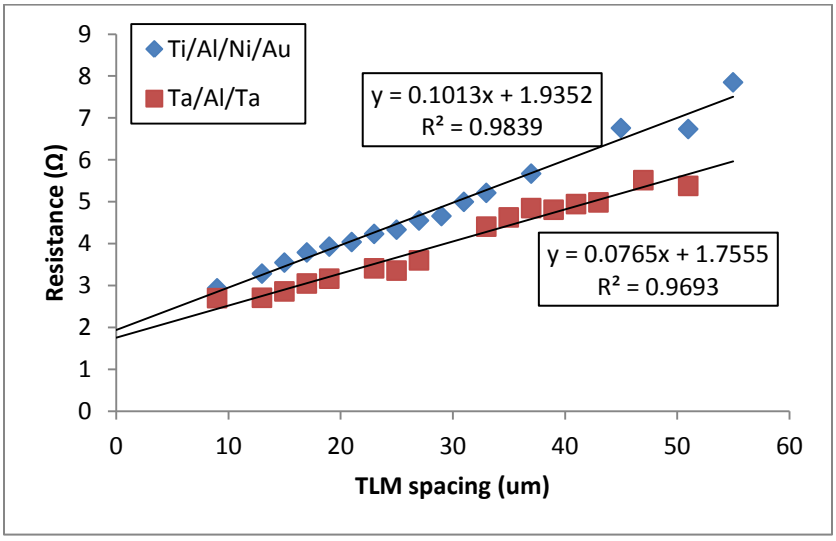

Figure 14: TLM plot for contact resistance extraction for Au-based and Au-free baseline contacts to GaN

Table 2: Comparison of Au-based and Au-free baseline contacts

	Au-based	Au-free
sheet resistance (ohm/sq)	85.092	64.26
contact resistance (ohm.mm)	0.8127	0.7373
contact resistivity (ohm.cm^2)	7.76E-05	8.46E-05
Transfer length (cm)	9.55E-04	1.15E-03

From calculation, the transfer length is much less than the minimum length of the 30um contact pad. Hence, current crowding effects are negligible. Both the Au-based and Au-free contacts have very similar contact resistance and either of them can be used for the fabrication of TiN and TaN diodes. The fact that Ta/Al/Ta is Au-free, requires lower temperature anneal and has a comparable contact resistance to the Au-based stack it is chosen as the ohmic contact stack for the fabrication of TiN and TaN diodes.

3.3. Characterization of TiN and TaN schottky diodes

Now consider step 3.2(ii), the fabrication of TiN and TaN schottky diodes. Once ohmic contacts are fabricated, using a 2^{nd} mask, windows are defined using a bi-layer liftoff photolithography process. TaN and TiN are evaporated (on separate samples) using e-beam evaporation. J-V characteristics are measured in the dark, as-deposited and after RTA in the range 300 ^{o}C to 1100 ^{o}C with steps of 100 ^{o}C in vacuum.

3.3.1. Barrier height extraction procedure under forward and reverse bias

J-V characteristics were analyzed for the barrier height extraction in both the forward and reverse bias characteristics. For the forward bias, the following analysis procedure was used. For a metal-semiconductor junction in forward bias, the expression for current density can be written in the form

$$J = J_0 \exp\left(\frac{qV}{nk_BT}\right) \quad (3.2)$$

Where V is the applied forward bias across the junction, n is the non-ideality factor and J_0 is the reverse saturation current. By taking log of the expression above, we get

$$\ln J = \ln J_o + \frac{qV}{nk_BT} \quad (3.3)$$

Hence by plotting $\ln J$ versus the sweeping voltage V and extrapolating to V =0, the reverse saturation current J_0 can be obtained. The slope of the curve gives the non-ideality factor n. Once the reverse saturation current is obtained, the barrier height can be obtained from expression

$$\phi_B = \frac{k_BT}{q}\ln\left(\frac{A^*T^2}{J_0}\right) \quad (3.4)$$

Analysis under reverse bias is not as straight forward as in forward bias. Once the analysis is complete, though, the barrier height and the doping concentration at the metal-semiconductor interface can be determined. From Padovani and Stratton's analysis [30] using a field-thermionic emission model of under reverse bias, the J-V characteristics was simulated for different doping concentration and barrier height. Figure 15(a) and (b) show the simulated J-V characteristics in reverse bias for different

barrier heights and different doping concentrations respectively. It is clear that a change in the slope of the reverse bias characteristics indicates a change in doping and a shift in the intercept indicates a change in barrier height. Hence by carefully fitting the measured J-V characteristics to the simulated curve, both barrier height and the doping concentration can be extracted.

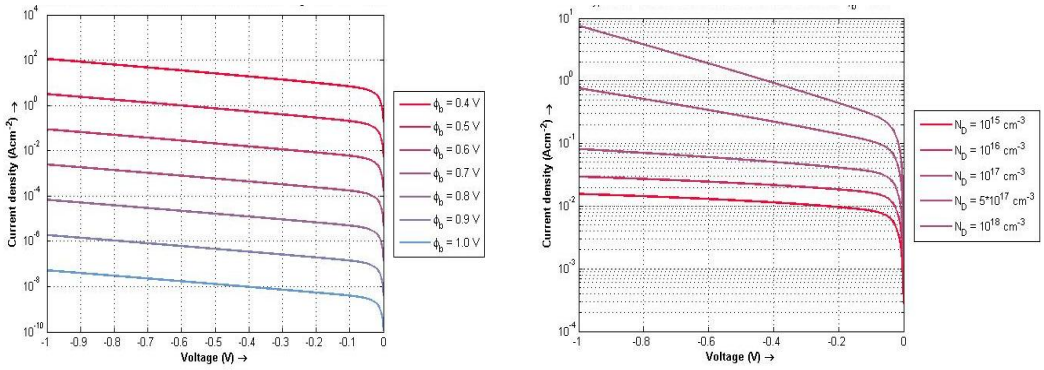

Figure 15: (a) and (b) show the J-V characteristics of metal-semiconductor junction in reverse bias for different barrier heights and for different doping respectively

3.3.2. Analysis of TiN schottky diode

Figure 16 shows the J-V characteristics of TiN schottky diode as-deposited and at different anneal temperatures. After analyzing the curve at forward bias using the procedure described in 3.2.1, the barrier height at different anneal temperatures is extracted and is shown in Figure 17.

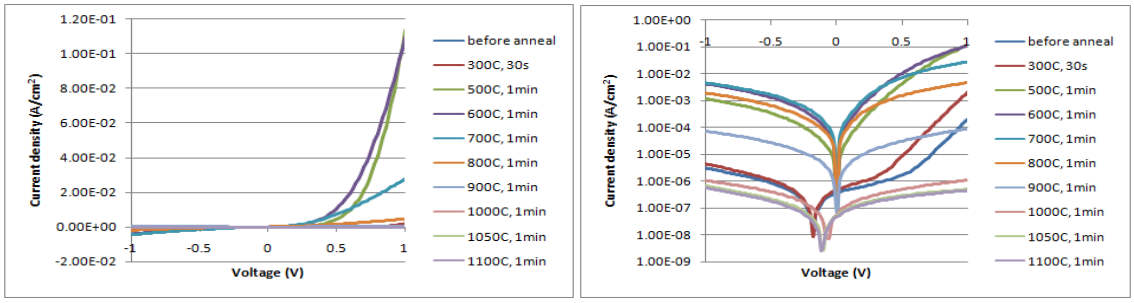

Figure 16: J-V characteristics in (a) linear and (b) log scale over a RTA range [300, 1100 ^{o}C].

It can be seen that the barrier height is least after a RTA of 700 ^{o}C. The change in the trend of barrier height is indicative of a transition to a new phase of TiN, which is also apparent from the change in color of the diode structures as shown by the light microscopic image of Figure 18. A transition of color from an as-deposited color of pinkish white to bluish green after RTA 800 ^{o}C and then to green after 900 ^{o}C RTA is observed. The barrier height saturates for anneal temperatures greater than 1000 ^{o}C.

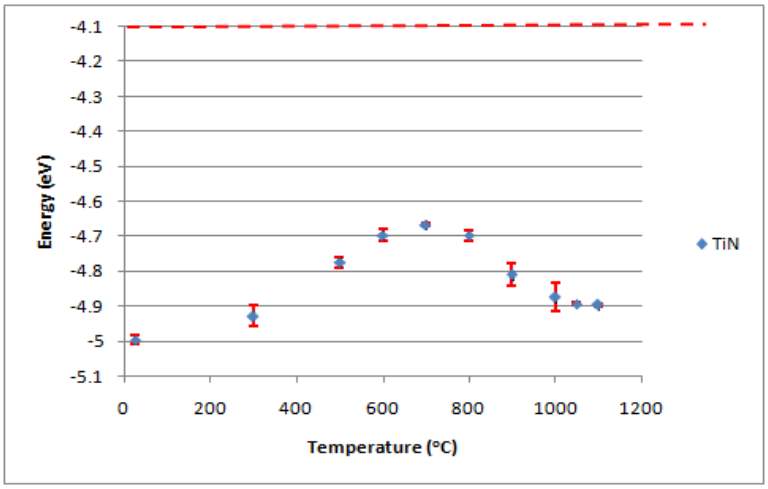

Figure 17: Barrier height extracted from forward characteristics of TiN schottky diode.

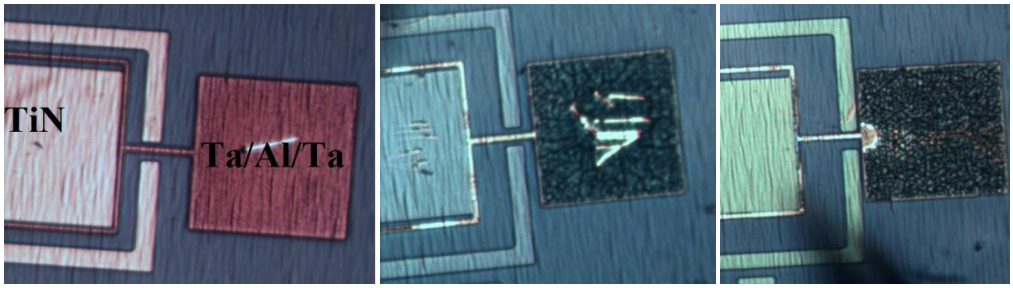

Figure 18: Light Microscopic image of TiN schottky diode (a) as deposited (b) after RTA 800 ^{o}C, 1min (c) after RTA 900 ^{o}C, 1min.

Analysis under reverse bias can act as a check for the validity of the analysis during forward bias. More importantly, as discussed earlier, it not only gives the barrier height, but also gives the doping at the metal nitride-GaN interface. The reverse bias characteristics over a bias range 0.3V to -1V is shown in Figure 19.

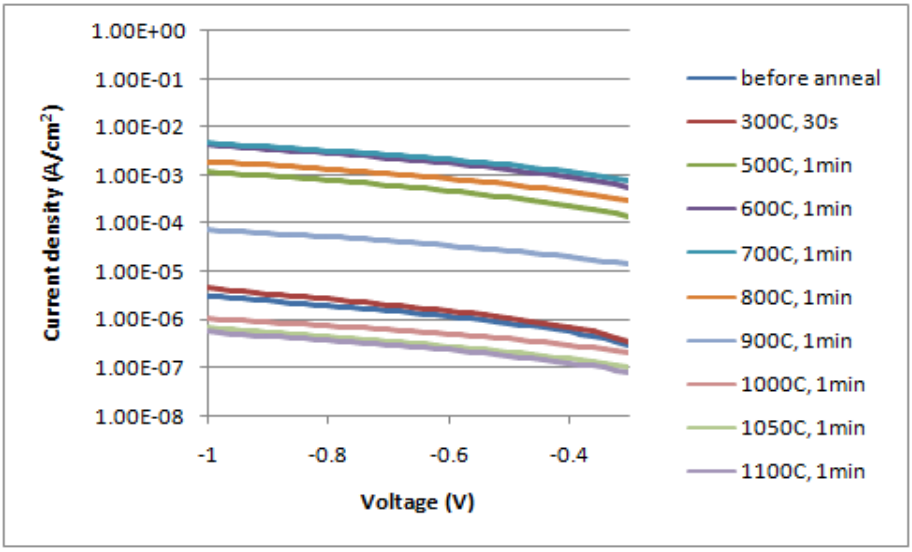

Figure 19: The reverse bias characteristics of TiN schottky diode measured after different temperature anneals over a bias range of -0.3V to -1V.

By fitting the slope and intercept of the J-V characteristics to thermionic-field emission model discussed in 3.3.1, we obtain the barrier height and the corresponding doping information as shown in Figure 20. It can be observed that the trend in the barrier height in forward bias agree with that under reverse bias. This compliance proves the validity of both extraction schemes.

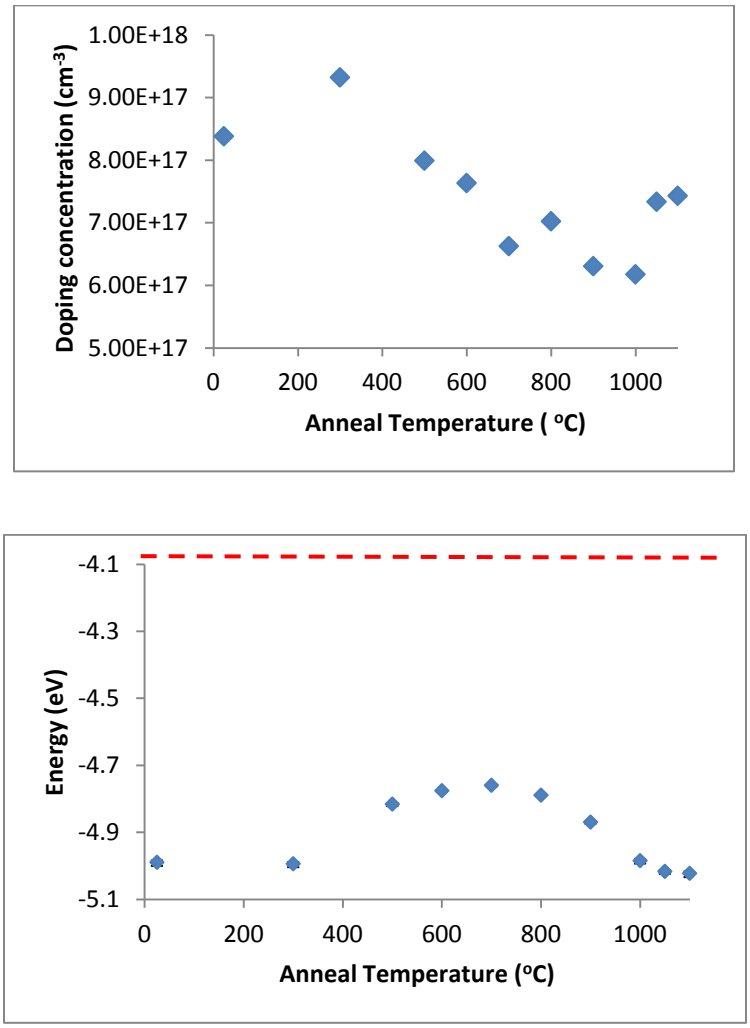

Figure 20: Extracted barrier height and the corresponding doping concentration at the metal semiconductor interface at different anneal temperatures.

The doping concentrations at the interface calculated for the entire anneal spectrum fall within the range of $6 \times 10^{17} to\ 9.5 \times 10^{17}$ cm^{-3}. From the simulations in section 2, it is clear that changes in doping concentration at the metal-semiconductor interface change the barrier width. Hence this very small variation in doping concentrations proves that the barrier width remains almost constant over the entire anneal range. Moreover, this also shows that the out-diffusion of N from GaN to the metal-nitride is negligible. (A slight decrease in doping concentration is suggestive of out diffusion of N from TiN into GaN) Hence the change in the current density is predominantly due to the reduction in barrier height with the barrier width held constant.

3.3.3. Analysis of TaN schottky diode

TaN schottky diodes were analyzed in the same manner as TiN diodes. The J-V characteristics over a RTA range of 300 ^{o}C to 1100 ^{o}C range is as shown in Figure 21.

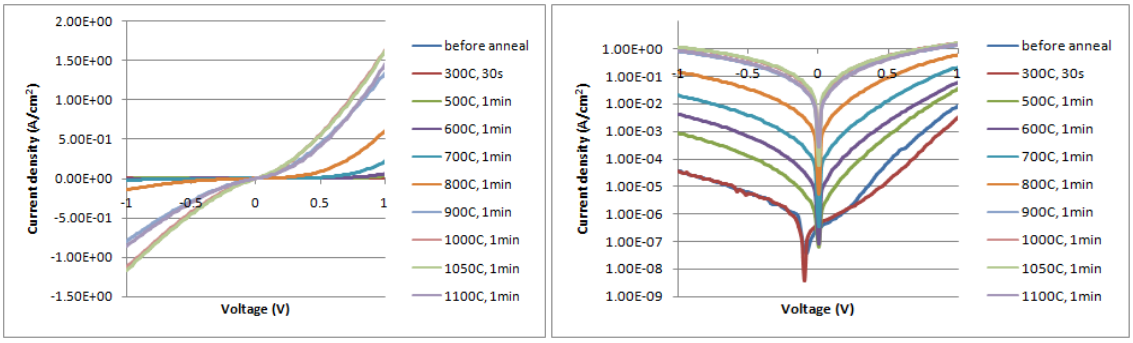

Figure 21: J-V characteristics of TaN schottky diodes over a wide RTA range (a) in linear scale (b) in log scale.

From analyzing the forward bias characteristics, the barrier height can be extracted as shown in Figure 22. It can be seen that the extracted barrier height decreases constantly up to 900 ^{o}C anneal and saturates at higher anneal temperatures. Unlike TiN, the trend of the barrier does not indicate any phase transition of TaN. Moreover, there is no change in color under the microscope which further supports the fact that TaN does not change phase during the annealing process.

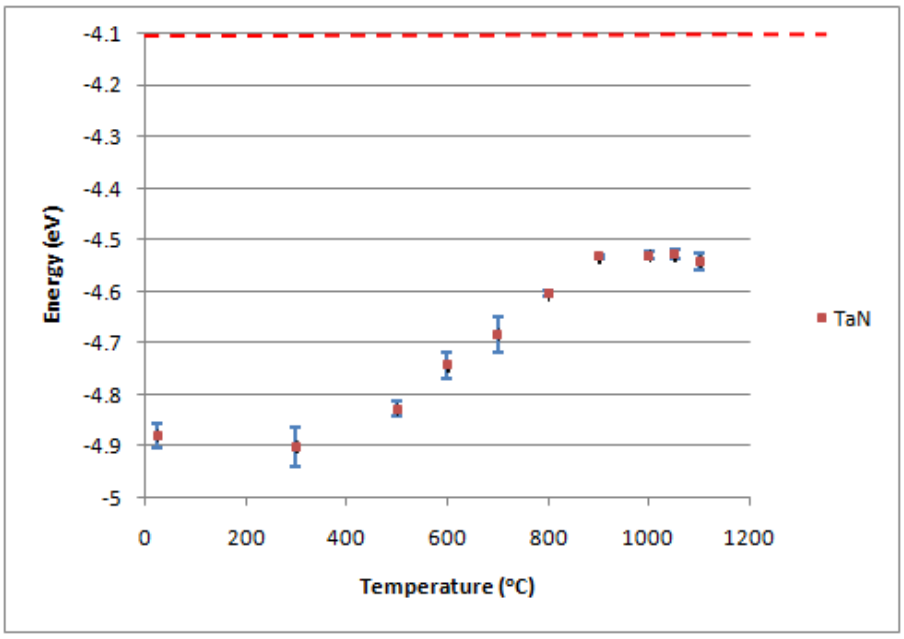

Figure 22: Extracted barrier height of TaN schottky diode obtained from the forward bias characterstics after RTA at different temperatures.

Figure 23 shows the barrier height and interface doping concentration extracted from the reverse bias characteristics. Like TiN, both the extraction schemes comply with each other which is apparent from the trend of barrier height with temperature.

The variation of doping with anneal temperatures is very similar to that of TiN. From the fact that the doping concentration is contained in a small range of $5.5 \times 10^{17}\ to\ 1.3 \times 10^{18}$ cm^{-3}, one can infer that the change in the current density is primarily due to the change in the actual barrier height with the barrier width remaining fixed. Also, this means that the out diffusion of N from GaN into TaN is negligible. In fact, the slight decrease in doping with increasing anneal temperature is suggestive of the fact that a little of N has out-diffused from TaN into GaN. Again, just like TiN, TaN is known to be an excellent diffusion barrier [31]. This can possibly explain why it is hard to out-diffuse N from GaN into TaN or TiN.

The analysis of barrier heights of TaN and TiN improved the understanding of ohmic contact to GaN in the following manner. Firstly, it can be noticed that neither TaN nor TiN is ohmic even after a 1100 ^{o}C anneal. This in turn means that TiN and TaN cannot be used directly for making ohmic contacts to GaN. (TaN and TiN have received a lot of attention as a potential ohmic contact due to its very high melting point, making it attractive for extreme temperature applications.) Secondly, the very small variation of doping concentration at the interface is suggestive along with the fact that contacts were rectifying is suggestive that low barrier width is crucial for ohmic behavior. In other words, the out diffusion of N from GaN is extremely important for achieving ohmic behavior in GaN. Hence as a next step, contacts which form a nitride at the surface during deposition or annealing is the favored candidate for ohmic contacts to GaN.

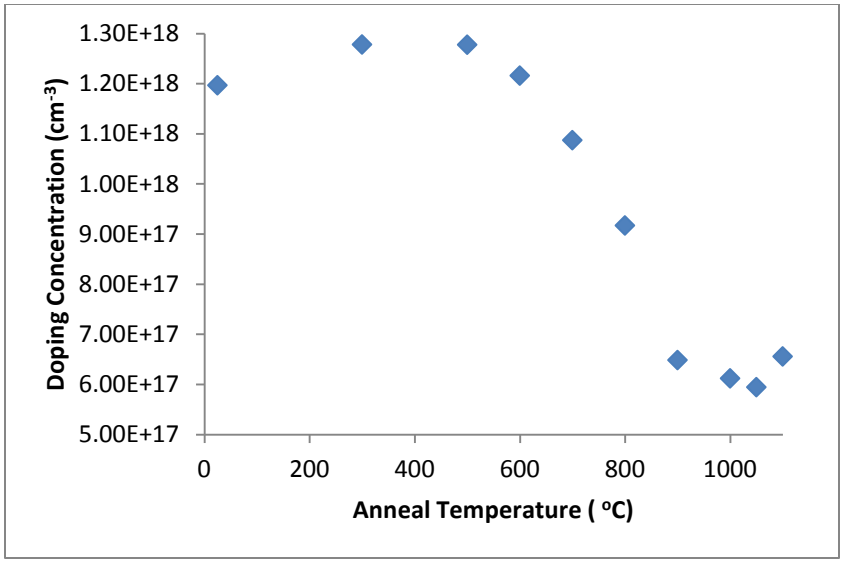

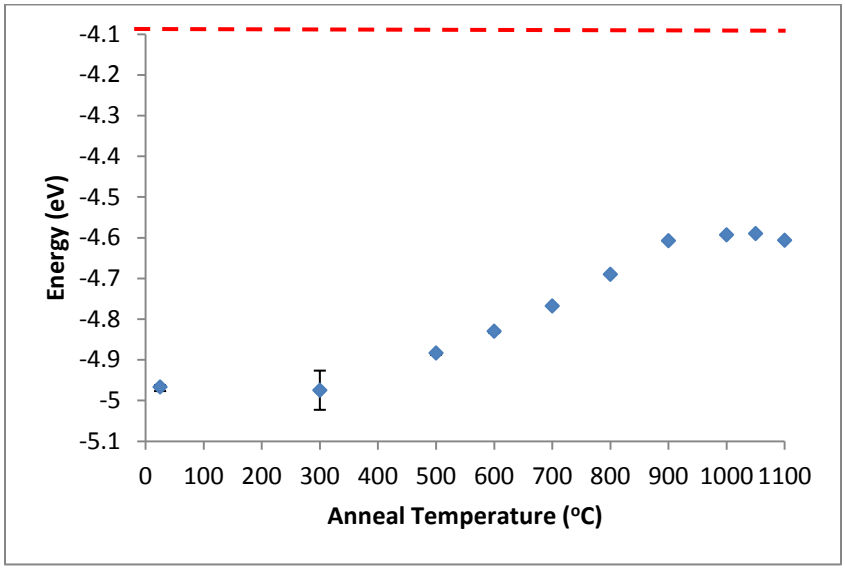

Figure 23: Extracted barrier height and doping concentration from analyzing the reverse bias characteristics of TaN schottky diode

3.4.Co-sputtered ohmic contacts to GaN

Co-sputtered Ta and Ti contacts with varying composition were used on GaN as ohmic contacts. The following steps were required for the testing of Ta_xTi_{1-x} contacts on GaN

(i) Sputter characterization at different operating powers of Ti and Ta

(ii) Solving for operating power using a linear sputter power vs deposition rate model

3.4.1. Sputter characterization of Ti and Ta

An operating pressure of 5mT was chosen for the sputter characterization of Ti and Ta. Silicon samples were degreased, dehydrated and loaded into the DC sputtering tool with scotch tape running through the center of the sample. After deposition, the scotch tape was carefully removed to create a step. Sputtering was done at three different powers, with two different times at each power. A profilometer was used to measure the thickness and calculate the individual deposition rates. Figure 24 shows the deposition rate versus power for Ti and Ta at different deposition rates. Note that the deposition rate of Ta is much greater than that of Ti. This is because Ta target was installed in a source with a high strength magnetic which inturn lead to an increased deposition rate. Note that deposition rate is treated to be a linear function of power in the range of interest. The linear fit shown in the plot was used to predict the deposition rates at other operating pressures.

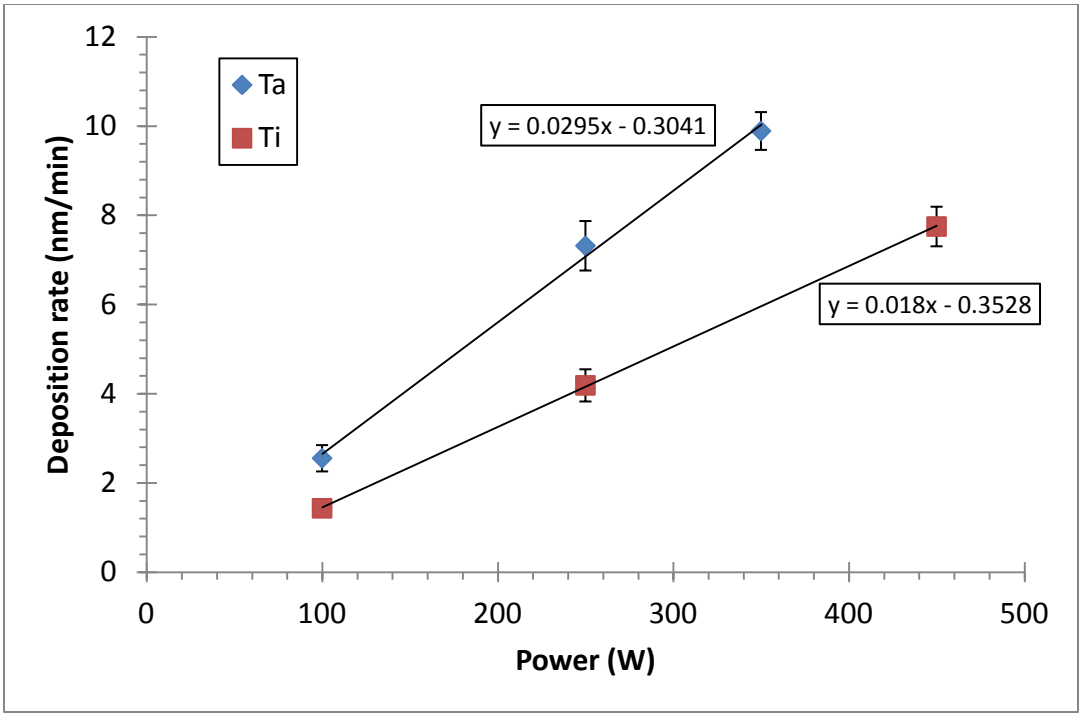

Figure 24: Sputter characterization of Ti and Ta targets at an operating pressure of 5mT

3.4.2. Method to find the operating power for different Ti and Ta compositions

During co-sputtering the composition 'x' in $Ta_xTi_{(1-x)}$ can be found out from the following expression,

$$\frac{x}{1-x} = \frac{Flux\ of\ Ta}{Flux\ of\ Ti} = \left(\frac{R_{Ta}}{R_{Ti}}\right)\frac{\rho_{Ta}M_{Ti}}{\rho_{Ti}M_{Ta}} \qquad (3.5)$$

Where $R, \rho\ and\ M$ denote the rate of deposition, mass density and molar mass respectively. Using eqn (3.4) and the linear fit of power vs deposition rate, sputter power of Ta can be linearly related to the sputter power of Ti at every composition. This is shown in Figure 25 for various values of composition 'x'. Now, one more equation is necessary to solve for the exact sputter powers for Ti and Ta for obtaining a particular

composition. This can be obtained in several ways; one of the ways is to hold the net sputter deposition rate constant between the different compositions. A fixed deposition rate, R_0 = 7.5 nm/min is chosen as indicated by the line with negative slope in Figure 25.

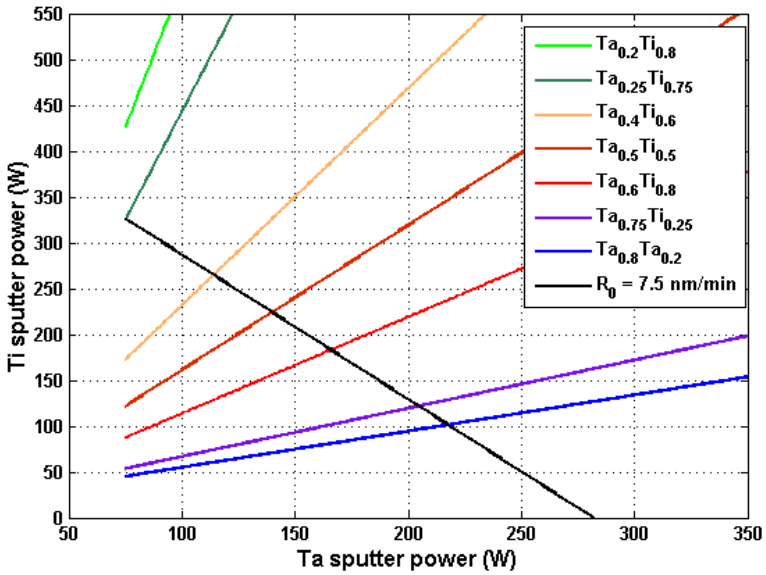

Figure 25: The method to obtain the points of operating powers for Ti and Ta deposition to obtain the required composition

The points of intersection of the line given by R0 = 7.5 nm/min with the other lines that correspond to different compositions of Ta-Ti alloy decide the operating points for the deposition of $Ta_xTi_{(1-x)}$ at a particular composition.

The experiment splits shown in Table 3 were conducted with the composition 'x' varying from x = 1 to x = 0 in steps of 0.25 as tabulated in table. The thickness of deposition for all samples was 50nm.

Table 3: Ta and Ti sputter power to obtain different composition of Ta-Ti alloy

composition	Ta sputter power	Ti sputter power	Constant parameters
Ta	269	0	Thickness = 50 nm Pressure = 5 mTorr No substrate heating Substrate rotation 20 rpm
$Ta_{0.25}Ti_{0.75}$	75	325	
$Ta_{0.5}Ti_{0.5}$	140	223	
$Ta_{0.75}Ti_{0.25}$	206	121	
Ti	0	375	

3.4.3. Fabrication and characterization of Ta_xTi_{1-x} contacts to GaN

Enclosed TLM patterns using the standard bi-layer liftoff resist were defined using photolithography. A dilute 1:10 HCl clean was done prior to metal deposition. Co-sputtering was done as discussed in section 3.3.2, followed by liftoff to obtain the desired TLM structures.

The devices were all perfectly ohmic, both as deposited and at different anneal temperatures. Four point probe measurements were taken in the dark at room temperature and contact resistance was extracted at anneal temperatures ranging from

400 ^{o}C to 600 ^{o}C as shown in Figure 26. As deposited, the contact resistance is the minimum for $Ta_{0.25}Ti_{0.75}$. However after a 600 ^{o}C anneal, we see that the contact resistance of Ta takes the least value. Also note that Ta contacts have the maximum change of contact resistance from as deposited to after 600 ^{o}C RTA. This is clear from Figure 27 which compares the contact resistance of the various compositions on the same graph.

The specific contact resistivity was calculated using eqn (B 2) and is plotted for different compositions as shown in Figure 28. The following important inferences can be made at this point. All the co-sputtered contacts except Ta have roughly a magnitude of $\rho_c = 1 \times 10^{-3}\ \Omega cm^2$ in the anneal range of 400 ^{o}C to 600 ^{o}C. Ta has a minimum contact resistivity $\rho_c = 8.60 \times 10^{-5}\ \Omega cm^2$ after a 600 ^{o}C RTA. Hence it can be concluded that for the co-sputtered Ta_xTi_{1-x} contacts, x=1 is the optimum choice. After a 600 ^{o}C RTA, Ta contact drops down in contact resistance by an order of magnitude, making its contact resistance comparable to the Au-free baseline (Ta/Al/Ta). Note that the Au-free baseline was annealed at 575C, value close to 600 ^{o}C, where the least value of contact resistivity to Ta contact is observed. Hence it can be concluded that Al in the Ta/Al/Ta stack plays a much lesser role than the interface metal Ta itself in lowering the contact resistance.

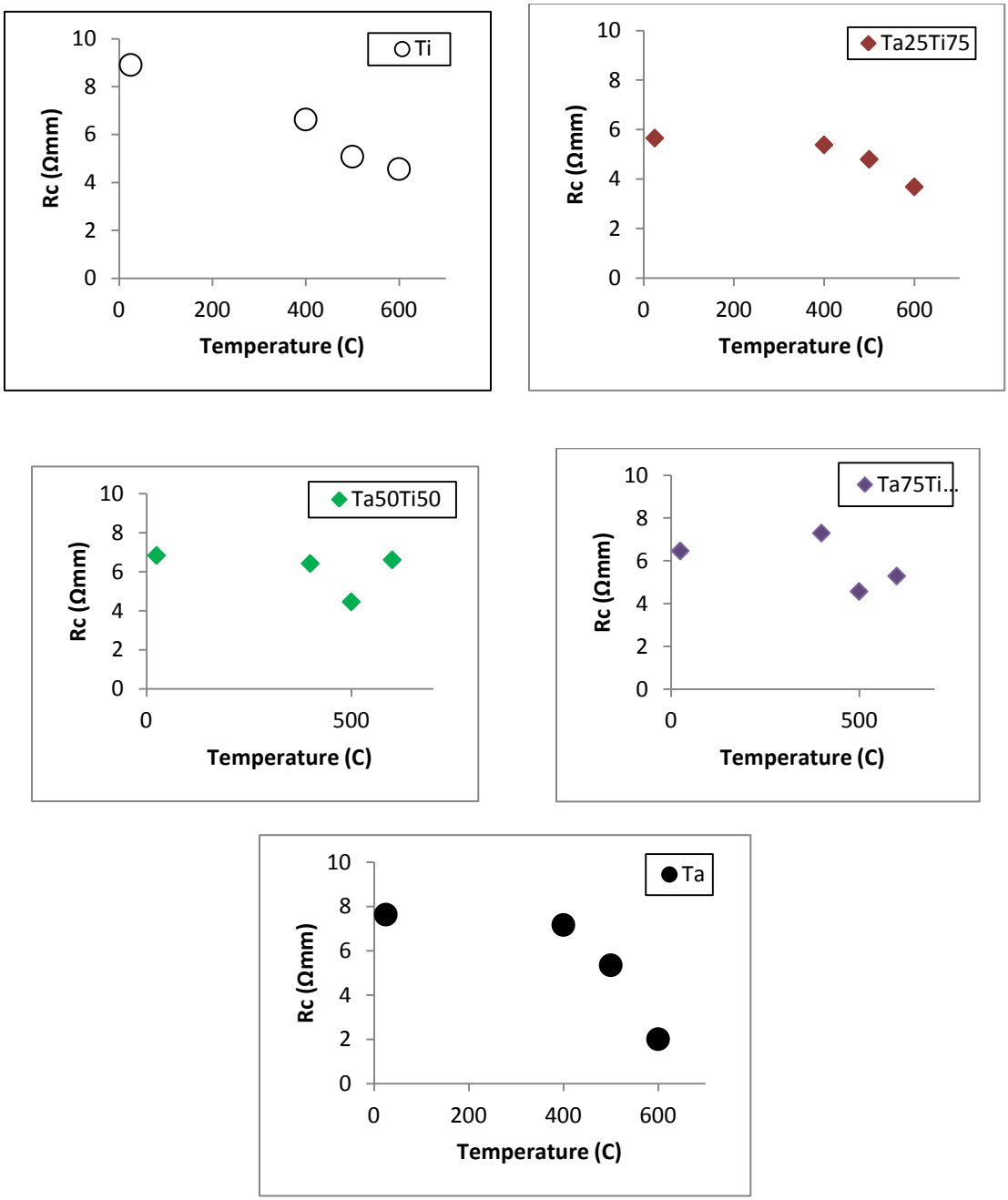

Figure 26: Extracted contact resistance of the sputtered contacts at different anneal temperatures

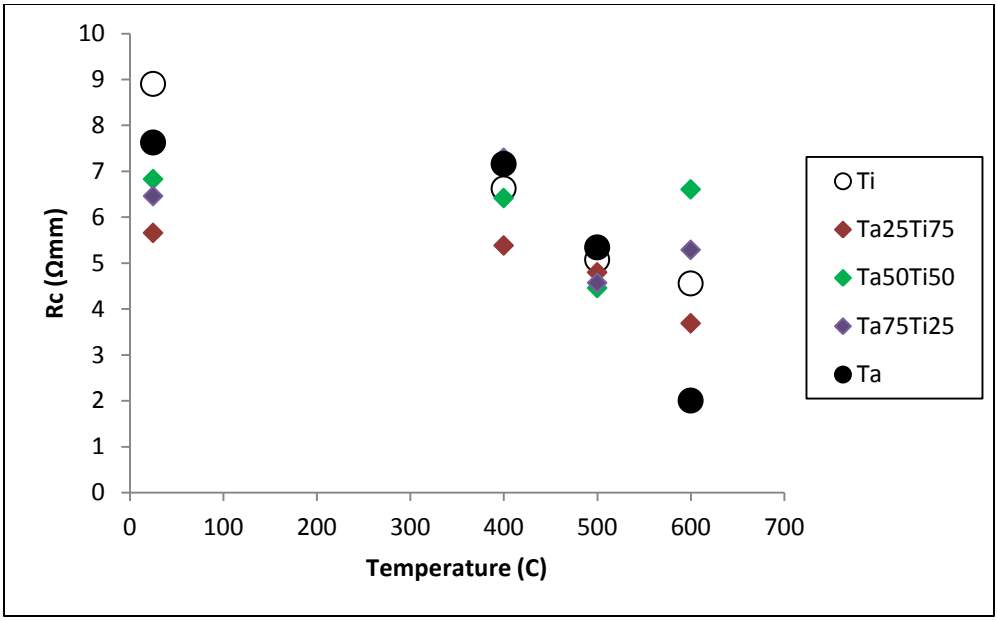

Figure 27: Contact resistance of the co-sputtered contacts compared at after each RTA.

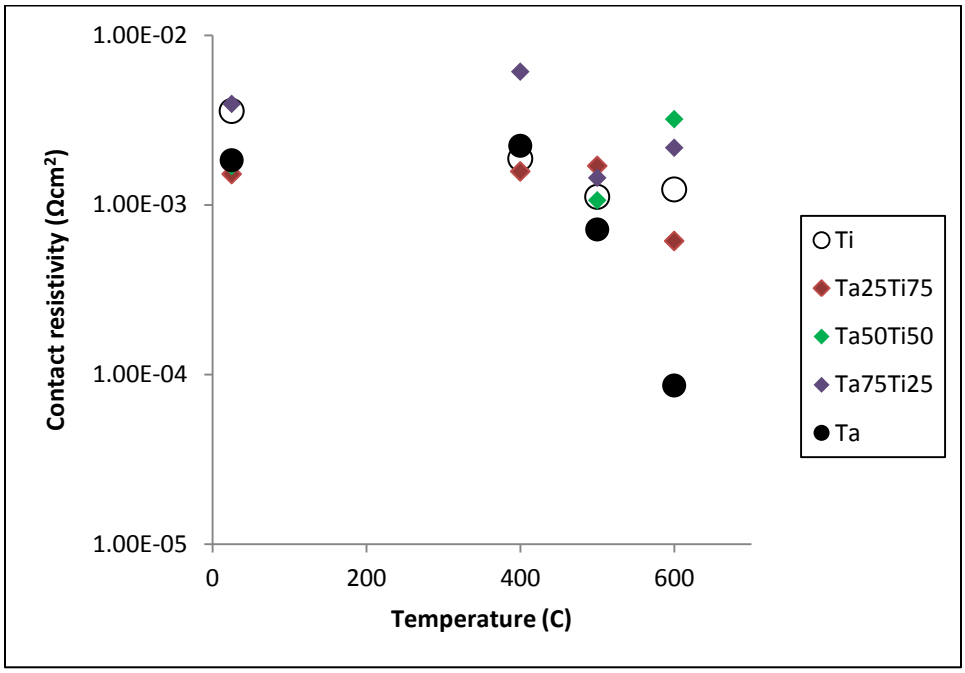

Figure 28: Specific contact resistivity of co-sputtered Ti-Ta contact calculated after RTA at different temperatures

4. AU-FREE SCHEME FOR GRAPHENE

4.1. Survey of ohmic contacts to graphene

Ohmic contact metallization schemes have been explored for CVD-grown graphene[32, 33], epitaxial graphene on SiC[12, 14, 34, 35] and mechanically exfoliated graphene flakes [13, 36-38]. CVD-grown graphene is promising as it allows growth on relatively large areas and can be transferred to any substrate of interest. Contact metallization schemes to CVD-grown graphene and epitaxial graphene on SiC have been Au-based thus far. The metal stack takes the form M/Au where M is the initial layer, typically 10 nm thick, [12] have been explored with various work functions for the intial layer M and have found Ti to be the favourable metal. Moon et al. [14] make use of Ti/Pt for their initial metal layer in the stack. Even though there is significant difference in the initial metal layers between the various contacts in literature, all of them make use of a thick Au capping layer. The purpose of Au, apart from the fact that it prevents the diffusion of impurities from diffusing into metal layers underneath is unknown.

To make use of the properties of graphene in a cost effective manner in the future would mean the need to make all the processes compatible with the existing CMOS technology. The ability to grow graphene by CVD and transfer to a substrate of interest makes high-volume production feasible. However, Au-free contact metallization schemes are required to meet the strict contamination rules of a CMOS processing line. Hence Au-free metallization schemes on CVD grown graphene is necessary in the near future. In a transistor process flow, different modules undergo different amounts of thermal budget, so the stability of a module under different temperatures should be explored.

Graphene surface treatment before metallization has proven to drive down the contact resistance and is still under research. Robinson eta al. [12] explore the effect of low power oxygen plasma and show that the contact resistance can be reduced by orders of magnitude. Hsu et al. [32] make use of a sacrificial layer of AlO_x to ensure that graphene does not contain photoresist residue and show significant improvement in contact resistance. Li et al [33] makes use of UV treatment and, again, show significant improvement in contact resistance. It should be noted at this point that the purpose of this work is twofold. Firstly, to understand the need for Au in contacting graphene and secondly, to design an Au-free contact based on this understanding. Reducing the contact resistance via various surface treatments is not the goal of the work. It is assumed that all the favourable impacts of graphene surface treatment still apply on the designed Au-free contact, but is beyond the scope of this work. Hence all the study on Au-free contacts will be done on untreated CVD grown graphene and compared to the same in literature.

4.2. Fabrication steps in achieving ohmic contacts to graphene

SiO_2 of 100 nm thickness was thermally grown on Si substrate at 1100 ^oC. Graphene was grown using CVD under optimized conditions on a Cu-foil and transferred to a SiO_2 substrate using a PMMA self-releasing layer. The procedure is shown in Figure 29 and was done by collaborating with Dr. Kyoung Lee of Texas State University.

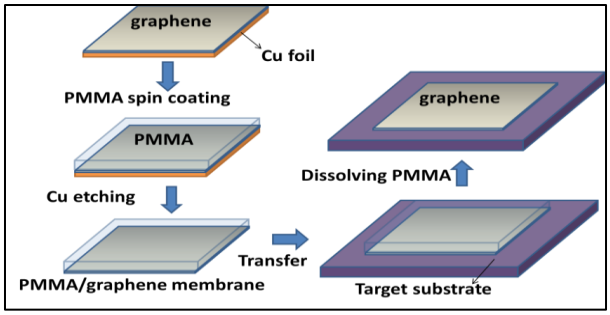

Figure 29: PMMA transfer method for transferring CVD grown graphene on to a substrate of interest. Reproduced from [39].

PMMA was removed by soaking in acetone for 30 min followed by a 400 ^{o}C anneal in N_2 ambience for 30 min. Contact windows of dimensions 206 x 206 μm^2 were defined using a bi-layer liftoff resist process. The metal stacks were deposited either via e-beam evaporation or DC sputtering. Henceforth, 's' in brackets indicated next to the metal film denotes a film that is sputtered, otherwise the film is evaporated. Figure 30 shows the final device cross section and TLM spacing (*d*), which was varied across the sample. Multiple metallization schemes were tested for contact resistance.

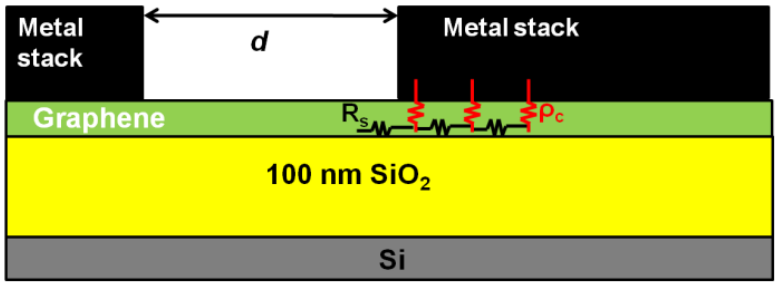

Figure 30: Cross section schematic of the final TLM structure with TLM spacing *d*.

The samples were processed in a rapid thermal anneal at temperatures ranging from 400 ^{o}C to 800 ^{o}C for 2 minutes in Ar ambience. The total resistance was measured before anneal and at each anneal temperature using four-point measurement. The contact resistance was extracted in the same procedure as explained in section 2.

4.3. Obtaining a Au-based baseline

Transfer line structures were fabricated using the Ti/Ni/Au (10/5/35 nm) stack and the contact resistance was extracted at different anneal temperatures as shown in Figure 31(a), (b).

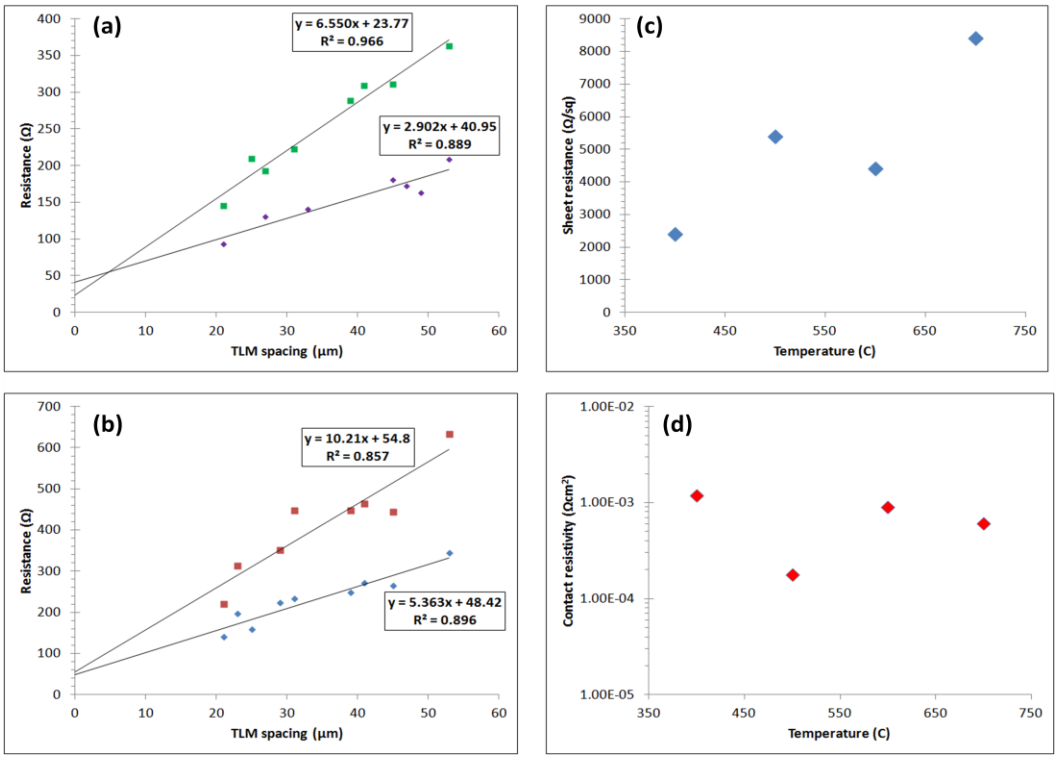

Figure 31: (a), (b) TLM plot for Ti/Ni/Au contact to graphene (c) Extracted sheet resistance and (d) calculated specific contact resistance after RTA at different temperatures

The specific contact resistance and sheet resistance at different anneal temperatures is shown in Figure 32 (c) and (d). Note that the minimum contact resistance is observed after a 500 ^{o}C anneal. The minimum value is around $2 \times 10 - 4$ Ωcm^2.The sheet resistance degrades at higher anneal temperatures indicative of decomposition of graphene under heat.

4.4. Challenges in achieving Au-free contacts

One of the potential challenges while making contact to graphene is metal delamination due to the internal stress of the metal stack. Figure 32 reproduced from [12] shows Al/Au contact delaminated due to stress relaxation. This happens in graphene because the atoms in a graphene lattice are sp^2 hybridized and hence there is no dangling bond in the z-direction that can bond with the metal on top. As a result, the force of attraction between the graphene and metal is inherently weak (Van der Waals forces) leading to delamination if the internal stress is high enough.

Therefore the internal stresses in the metal thin films become an extremely important design consideration. Figure 33 (a) shows the light microscope and an SEM image of Ti/Ni, relaxed due to high residual tensile stress. Figure 33 (b) shows Ti/Ni/Al(s)/Ta(s), relaxed due to high residual compressive stress.

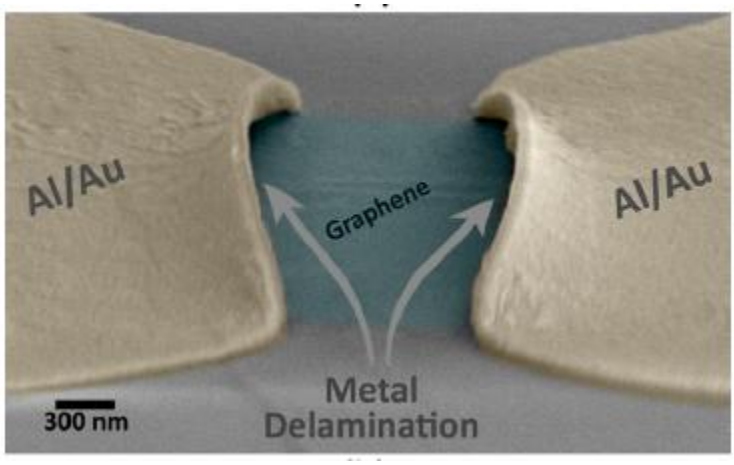

Figure 32: Metal delamination due to high compressive internal stress. Reprinted with permission from [12] (Copyright [2011] by American Istitute of Physics).

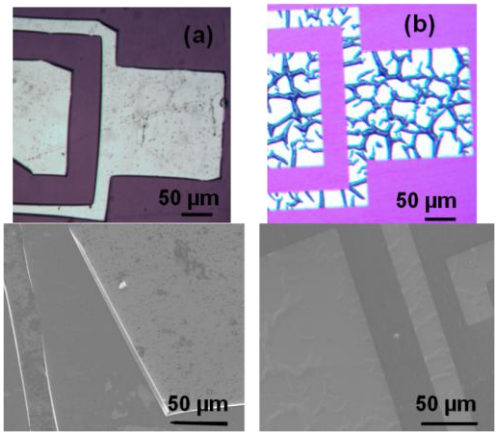

Figure 33: (a) shows light micrograph and a secondary electron SEM image of a Ti/Ni film on graphene relaxed due to high tensile residual stress (b) shows a Ti/Ni/Al(s)/Ta(s) film relaxed due to high compressive stress

The next design consideration is stress relaxation due to the process of annealing. Thermal budget in future devices integrated with graphene is unknown and hence it is important that ohmic contacts to graphene can withstand high temperature anneals. Figure 34 (a) and (b) show a light microscope image of $Ti_{0.5}Ta_{0.5}$/Ta film after a 400 ^{o}C,

2min RTA and Ta/Ti/Ta film after 500 ^{o}C, 2min RTA respectively. Clearly, the images indicate that stress relaxation has occurred during annealing, hence losing physical contact with graphene.

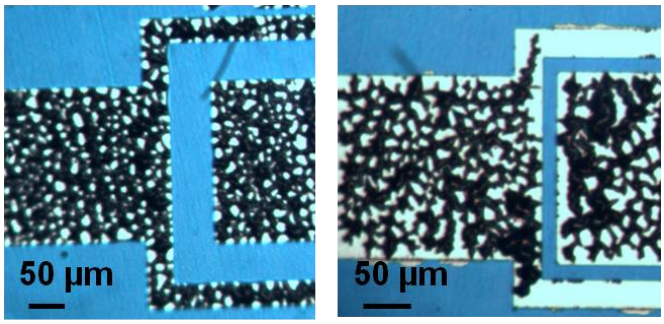

Figure 34: (a) shows light micrograph of a $Ta_{0.5}Ti_{0.5}$(s) /Ta film on graphene relaxed after a 400 ^{o}C anneal (b) shows a Ta/Ti/Ta film relaxed after a 500 ^{o}C anneal

Ti/Ni/Au, the Au-based baseline used in this study, complies with both the design considerations – the overall stress in the film is not high enough to cause delamination during liftoff and stress relaxation does not occur during annealing over a wide temperature range. The reason why most Au-based based (exception: Al/Au discussed in [12]) satisfy both the design considerations is not clear at this point. The following sub-section explores the reason behind success of Au-based contacts in this regard. Au-free contacts can be designed based on this understanding.

4.5. Stress measurement in metal thin films

Samples were prepared for metal thin film stress measurement in the following manner. 2" Si substrates were deposited with 100 nm PECVD silicon oxide served as the bare sample. Different metallization schemes as tabulated in Table 4 were deposited on top of

silicon dioxide. The samples were shipped to Toho Technologies Inc and the stresses in metal films were measured using FLX 2320-S, a thin film stress measurement system that calculates stress by measuring the radius of curvature of wafers. The measurements were made at room temperature.

Table 4: Samples prepared for Flexus measurement

Film	**Thickness (nm)**
Ti/Ni	10/5
Ti/Ni/Au	10/5/35
Ti/Ni/Al/Ta	10/5/30/10
Ti/Ni/Al/Ta	10/5/80/10

Figure 35 (a) shows the overall stresses of the different metal stacks tabulated in Table 4. Ti/Ni stack has an overall tensile stress and Ti/Ni/Au stack has an overall compressive stress. Clearly, from a differential analysis of these two films it can be concluded that Au has a compressive internal stress component, as indicated by the decoupled stress versus thickness diagram, Figure 35 (b). Note that the dotted lines in Figure 35 (b) indicate a first order approximation of the residual stress for other thicknesses

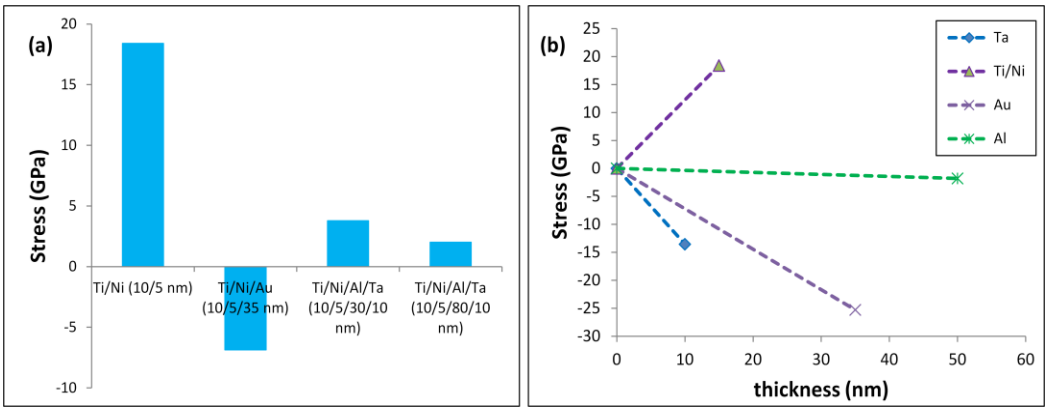

Figure 35: (a) overall residual stress of the different metal stacks tabulated in Table 4. (b) stress in the individual metal layers obtained after decoupling the data in (a)

Hence it can be seen that one of the roles of Au is to reduce the overall tensile nature of the first metal layer in the stack. This explains why Robinson et al [12] did not experience any issues with metal delamination for most of their Au-based contacts. However, [12] reported metal delamination for their Al/Au contact and this can be explained as follows. The residual stress in Al is low, but slightly compressive in nature as shown in Figure 35 (b). When two metal layers of compressive stress are used, the overall stress will add up leading to a high enough metal stress to cause delamination.

Coming to the second design consideration, viz., stress relaxation due to annealing, it can be noticed that Au-based contacts do not have this issue when annealed over a wide range of temperatures. This can be attributed to the high diffusivity of Au. When annealed at high temperatures, Au diffuses and intermixes well with the layer(s) underneath and hence expanding and contracting under thermal stress at the same rate.

4.6. Design and optimization of an Au-free contact

Al/Ta bilayer is chosen to replace Au. The purpose of choosing this bilayer to replace gold is justified as follows. It is studied in [40] that evaporated Al has a residual compressive stress of a low magnitude. This is also confirmed by Flexus measurements for aluminum as shown in Figure 35 (b). As a result, this allows the use of sufficiently thick Al layer for enabling probing without the introduction of too much residual stress. Due to its low melting point, Al is believed to have reasonably high diffusivities especially at higher temperature anneals. As a result, Al can intermix well with the different metal layers and hence help avoid stress relaxation during annealing as the overall structure will expand and contract as a single entity. The purpose of Ta cap is to serve as an oxygen diffusion barrier and prevent the oxidation of aluminum.

Figure 35 (a) shows the stress of two Au-free metal layers, Ti/Ni/Al/Ta with aluminum thicknesses of 30 nm and 80 nm respectively. From a differential analysis of Ti/Ni layer and the two different Au-free stacks, we can decouple the internal stress of Al and Ta, shown in Figure 35 (b). Firstly, it is clear that Al has a small compressive component to it and the Ta cap has a larger compressive component of stress. Together, it serves to replace the compressive nature of Au.

Now, let us design an Au-free contact stack based on the overall stress of the film. The capping Ta layer is fixed at 10 nm and the Ti/Ni bilayer is also fixed at 10/5 nm. The aluminum thickness ‘x’ has to be designed. The overall stress of Ti/Ni/Al/Ni layer can be expressed by the following empirical expression, approximately to the first order.

$$\sigma_{total} = \sigma_{Ti/Ni} + \sigma_{Al}\left(\frac{x}{50}\right) + \sigma_{Ta} \quad (4.1)$$

where $\sigma_{total}, \sigma_{Ti/Ni}, \sigma_{Al}\ and\ \sigma_{Ta}$ denotes overall stress, stress of Ti/Ni (10/5 nm) bilayer, stress of 50 nm aluminum and the stress of 10 nm Ta capping layer respectively. To avoid peeling during liftoff

$$|\sigma_{total}| \leq |\sigma_{Ti/Ni/Au}| \quad (4.2)$$

where $\sigma_{Ti/Ni/Au}$ is the overall stress of Au-based baseline. Solving for 'x' from equations 1.1 and 1.2, we find that 'x' can be as large as 300 nm. This justifies the point made earlier that Al has a low magnitude of stress making possible to form thicker metal stacks without increasing the overall stress of the film by a large extent.

As emphasized earlier, the overall stress of the film is just one of the design considerations. Now, let us consider the second equally important factor - stress relaxation during annealing. It is very hard to predict through simple models the effect of stress relaxation during annealing. Hence the optimum design has to be achieved through experiments. Table 5 shows an experiment split on three different Al thicknesses of 30 nm, 80 nm and 200 nm respectively. Figure 36 shows the effect of annealing at 400 ^{o}C for 2min on these samples. It is clear that stress relaxation leading to bubbling takes place in samples with thicker aluminum of 80nm and 200 nm. But however, it is clear that there is no stress relaxation for thinner, 30 nm Al. It is believed that Al intermixes well with other metal layers in the stack when a thinner 30nm layer is used leading to expansion and contraction of the film as a single unit. However when a thicker Al of 80 nm or greater is used, the intermixing between the layers is not

sufficient to achieve the same rate of thermal expansion and contraction between the different films, hence leading to stress relaxation.

Table 5: Experiment split to determine the optimum thickness of Al

Film	Thickness (nm)
Ti/Ni/Al/Ta	10/5/30/10
Ti/Ni/Al/Ta	10/5/80/10
Ti/Ni/Al/Ta	10/5/200/10

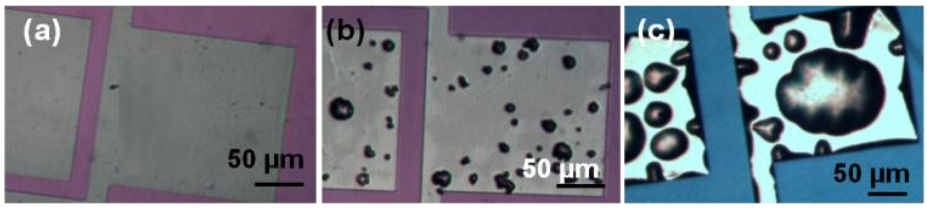

Figure 36: (a) shows a light microscope picture of Ti/Ni/Al/Ta (10/5/30/10) (b) Ti/Ni/Al/Ta (10/5/80/10) (c) Ti/Ni/Al/Ta (10/5/200/10) after a 400 ^{o}C RTA. For Al thickness of 80 nm and 200 nm we see bubbling of film due to compressive stress relaxation.

An important point to be noted here is that the overall stress in the metal stack will not help in predicting whether a particular stack would relax during RTP or not. This is apparent from the overall stress value of Ti/Ni/Al/Ta with different thickness of 30 nm and 80 nm of Al as shown in Figure 35 (a). We see that the overall stress of the film with thicker Al is lower, however there is significant stress relaxation leading to bubbling as indicated by Figure 36 (b).

At this point, it is clear that Au and now optimized Al/Ta (30/10 nm) serves two purposes. Firstly, due to their inherent residual compressive stress, both reduce the overall stress of the metal stack. Secondly, both prevent stress relaxation while annealing due to sufficient intermixing of the metal layers. At this point, the role of Au or Al/Ta in the contact resistance is still unclear. The following section explores the effect of Au in the contact resistance and compares the same with the optimized Au-free contact.

4.7. Characterization of the optimized Au-free contact and understanding the effect of Au on contact resistance

Figure 37 shows the TLM plot of Ti/Ni/Al/Ta (10/5/30/10 nm) on graphene after RTA at 400 ^{o}C to 800 ^{o}C. The sheet resistance can be extracted from the slope of the plot and the contact resistance can be extracted from the intercept of the plot. Clearly we see that the lowest contact resistance is obtained after a 500 ^{o}C RTA for 2 min. (highlighted in black)

Figure 38 shows the sheet resistance of the after a RTA from 400 ^{o}C to 800 ^{o}C. It should be noted that the sheet resistance does not degrade up to a 500 ^{o}C anneal. After a RTA of 55^{o}C and above, the sheet resistance starts degrading significantly. At 800 ^{o}C, the sheet resistance is pretty poor indicating possibly graphene dissociation. This inference is coherent to the fact that the scatter in the TLM plot (Figure 37) is also quite high at 800 ^{o}C.

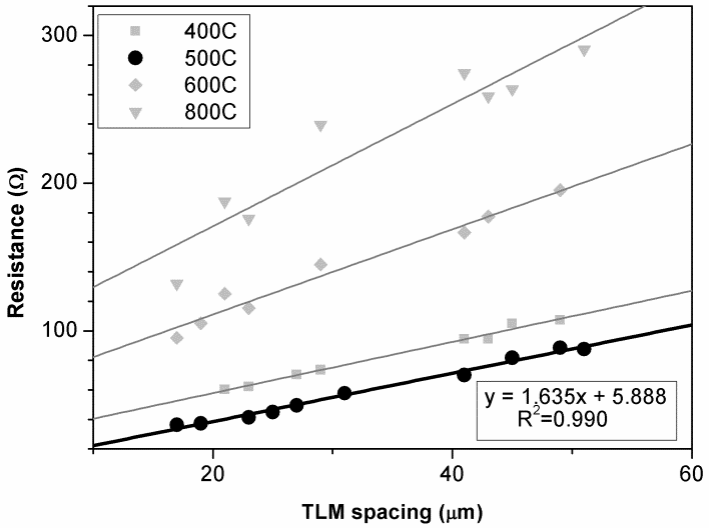

Figure 37: TLM plot of optimized Au-free Ti/Ni/Al/Ta contact on graphene measured after different anneal temperatures. Least contact resistance is observed after a 500 ^{o}C, 2min RTA

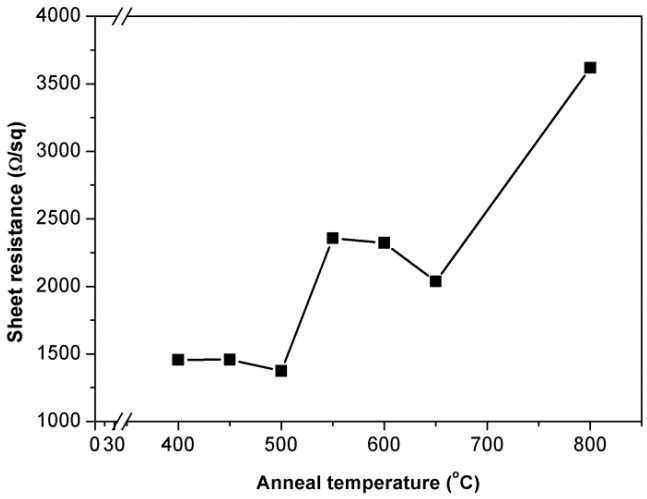

Figure 38: Sheet resistance of graphene extracted from the TLM plot of optimized Au-free Ti/Ni/Al/Ta contact after RTA at different temperatures.

Figure 39 shows the extracted contact resistance normalized to the total width at different anneal temperatures. The contact resistance has the least value after a 500 ^{o}C,

2min RTA. The values of contact resistance obtained for the Au-free contacts are comparable to untreated Au-based contacts to CVD grown graphene in literature [14, 41] as shown in Figure 39.

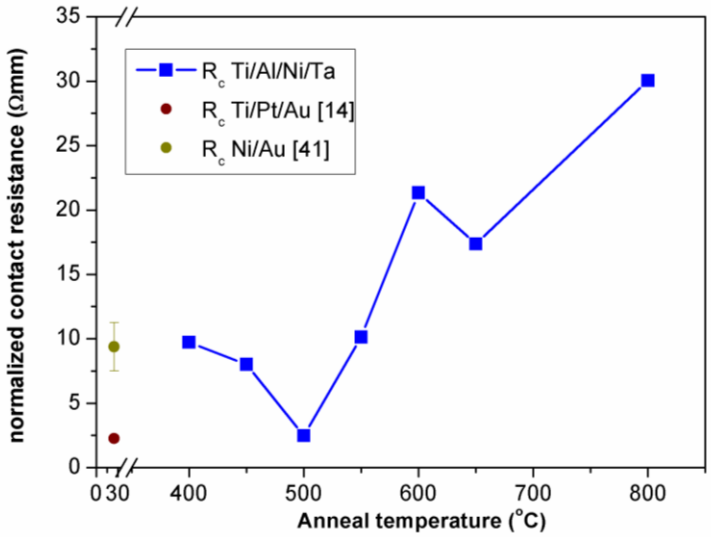

Figure 39: Contact resistance normalized by width is plotted at different anneal temperatures. Au-based contacts from literature for untreated graphene are compared.

Figure 40 shows the specific contact resistance of the optimized Au-free and Au-based baseline. Moreover, Au-based contacts from literature [12, 35] are also compared. For both the optimized Au-free and Au-based baseline, the minimum contact resistivity is observed after 500 ^{o}C RTA for 2min. The contact resistivity rises again and saturates after a 600 ^{o}C RTA. Hence, the rise in contact resistance above 600 ^{o}C RTA observed in Figure 39, is the effect of increasing sheet resistance with contact resistivity held constant.

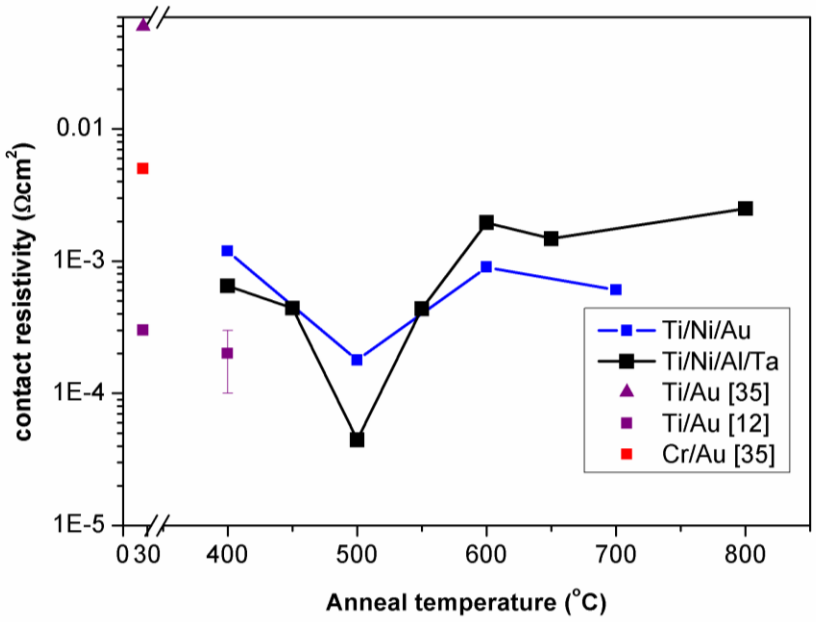

Figure 40: Specific contact resistance of the optimized Au-free contact compared with the Au-based baseline and other Au-based contacts to untreated CVD grown graphene in literature

The following important observation can be made at this point about the effect of Au in the contact resistance. The shape of specific contact resistivity for both the optimized Au-free contact and the Au-based baseline look very similar, with a minimum at 500 ^{o}C RTA. Hence, by replacing Au by Al/Ta, the trends of contact resistivity versus anneal temperature remains unaffected. Hence it can be inferred that Au has a negligible impact on the contact resistance. The initial metal layers, Ti/Ni, decide predominantly the contact resistance.

5. CONCLUSIONS AND FUTURE WORK

5.1. Conclusions from the present work

Energy band diagrams at equilibrium were simulated for different doping concentrations and barrier heights by numerically solving the Poisson equation. The solution indicated that larger doping concentrations and lower barrier heights were necessary to obtain a good ohmic contact. The fact that tunnelling current plays an important role in thinner barriers was illustrated by calculating the tunnelling probability at different doping concentrations. Significant transmission was observed for higher doping concentrations in the simulations. A mathematical model based on quantum mechanical transmission through an arbitrary barrier was developed for the computation of contact resistivity. This model was computationally simple as it only made use of parameters calculated at equilibrium. Moreover, it was applicable to all the GaN doping concentrations and metal work functions of interest because it did not make any common assumptions like depletion region or Boltzmann approximations. The contact resistivity simulations suggested that there was still a lot of room for improvement if it were possible to control both interface doping and barrier height effectively.

A better understanding of ohmic contacts to GaN was achieved by studying TiN and TaN schottky diodes. As the first step of fabrication of these contacts, the establishment of ohmic contact baseline to GaN was necessary. TLM measurements revealed that Au-free baseline contacts had comparable contact resistance to Au-based contacts with the added advantage of being Au-free. Hence the Au-free, Ta/Al/Ta contacts were used as the ohmic contact to TiN and TaN schottky diodes. J-V characteristics were analysed in

both forward and reverse bias to extract the barrier height and doping concentrations. The measurements were performed as-deposited and after series of RTAs ranging from 300 ^{o}C to 1100 ^{o}C. The analysis for TiN diodes revealed that it changed phase after around 700 ^{o}C RTA, indicated by both a change of trend in the barrier height versus anneal temperature curve and by the change of color under a light microscope. The analysis of TaN diodes revealed that the barrier height kept decreasing until a 900 ^{o}C anneal and obtained saturation. However, a very interesting observation was made about the doping concentration at the metal-GaN interface. It changed only by a very small amount for both TiN and TaN diodes. This in turn meant that the out-diffusion of N from GaN was negligible. In fact, a small decrease in doping concentration with anneal indicated that the N from TiN and TaN diffused into GaN. Therefore a study of TiN and TaN diodes concluded that N out-diffusion from GaN is necessary for ohmic contact formation in GaN and it could not be achieved by merely using TiN and TaN.

Co-sputtered Ta-Ti contacts were explored as a potential Au-free contact to GaN. The first step in achieving co-sputtered Ta_xTi_{1-x} was the characterization of the individual deposition rates of Ta and Ti at different sputter powers at a particular operating pressure. A linear fit was employed as a first order of approximation to predict the deposition rates at other sputter powers. Hence, the point of operation of the sputter powers for Ti and Ta to achieve a particular composition was calculated. TLM structures were fabricated for different compositions and studied at different anneal temperatures. As-deposited $Ta_{0.25}Ti_{0.75}$ showed the least contact resistance; however after a 600 ^{o}C RTA, Ta contacts had the minimum contact resistance, comparable to that of the Au-free

baseline Ta/Al/Ta. Hence x=1 turned out to be the optimum operating point for Ta_xTa_{1-x} contacts to GaN. Moreover, the fact that the contact resistivity of Ta contacts were comparable to Ta/Al/Ta baseline, suggested Al in Ta/Al/Ta played a very little role in the contact resistance. In other words, the contact resistance was dictated by the interface metal Ta.

Experiments on different Au-free metallization schemes to graphene revealed that the stress in the metal films played a very important role in its design. Contacts with high residual tensile or compressive stress lead to delamination, either after liftoff or during annealing. The stress becomes an important design consideration because of fact that C atoms in graphene are sp^2 hybridized and hence there are no dangling bonds in the z-direction to form covalent bonds with the deposited metal. Au-free contact metallization was successfully achieved to graphene by studying the role of Au in Au-based contacts. From stress measurements of different metal films, it was clear that Au had a high compressive stress component which decreased the overall stress of the Au-based stack. Also, Au based contacts did not show any indication of stress relaxation after RTA in the range [400 ^oC – 800 ^oC]. This is believed to be because of the high diffusivity of Au and hence leading to significant intermixing between the metals in the metal stack during annealing. Al/Ta served to replace Au due to the fact that its overall stress magnitude was comparable to that of Au-based contact and due to significant diffusivity of Al, it was possible to achieve enough inter-diffusion making it stable over a wide range of RTAs. The Au-free Ti/Ni/Al/Ta contact was optimized by observing the stability of contacts with different Al thickness. Next, the role of Au in the contact resistance was

studied by comparing the contact resistance with the optimized Au-free contact. It was observed that the contact resistance after all RTA was dictated by the interface metal Ti/Ni and Au had negligible impact on the contact resistance. Therefore Au plays an important role in the metal-graphene contact stability at a wide range of temperatures, but has negligible impact on the contact resistance. Now, an Au-free Ti/Ni/Al/Ta contact has been designed that successfully mimics the role of Au in Au-based contacts.

5.2. Future work

The idea of co-sputtering can be extended to study the effect of barrier height tuning on ohmic contacts on AlGaN/GaN heterostructures. Figure 41 shows the work function of AlN and TaN compared to the conduction band edge of AlGaN. By controlling the composition it is possible to tune the work function of co-sputtered Ta_xAl_{1-x} contact and match it to that of $Al_{0.24}Ga_{0.76}N$.

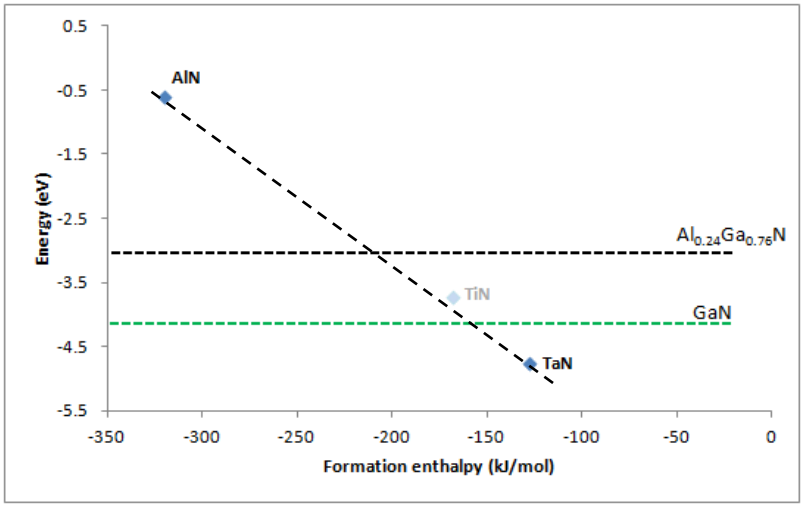

Figure 41: Work function of AlN and TaN compared with the conduction band edge of AlGaN. The dotted line can be achieved by the process of cosputtering Ta and Al

This work successfully eliminates the need for Au in ohmic contacts to graphene and GaN, while expediting the process of integrating the two materials with silicon electronics in a standard CMOS facility. Au-free ohmic contact technology to these materials can also be used to fabricate electronic devices comprised of GaN and graphene. Regardless of the application, this work provides a foundation for understanding ohmic contacts to GaN and graphene while utilizing metals and processes that are well established in the semiconductor industry.

REFERENCES

[1] L. Hyung-Seok, L. Dong Seup, and T. Palacios, "AlGaN/GaN High-Electron-Mobility Transistors Fabricated Through a Au-Free Technology," *Electron Device Letters, IEEE,* vol. 32, pp. 623-625, 2011.

[2] U. K. Mishra, P. Parikh, and W. Yi-Feng, "AlGaN/GaN HEMTs-an overview of device operation and applications," *Proceedings of the IEEE,* vol. 90, pp. 1022-1031, 2002.

[3] K. S. Novoselov, A. K. Geim, S. V. Morozov, D. Jiang, Y. Zhang, S. V. Dubonos, *et al.*, "Electric Field Effect in Atomically Thin Carbon Films," *Science,* vol. 306, pp. 666-669, 2004.

[4] K. S. Novoselov, A. K. Geim, S. V. Morozov, D. Jiang, M. I. Katsnelson, I. V. Grigorieva, *et al.*, "Two-dimensional gas of massless Dirac fermions in graphene," *Nature,* vol. 438, pp. 197-200, 11/10/print 2005.

[5] A. Reina, X. Jia, J. Ho, D. Nezich, H. Son, V. Bulovic, *et al.*, "Large Area, Few-Layer Graphene Films on Arbitrary Substrates by Chemical Vapor Deposition," *Nano Letters,* vol. 9, pp. 30-35, 2009/01/14 2008.

[6] Y. Zhu, S. Murali, W. Cai, X. Li, J. W. Suk, J. R. Potts, *et al.*, "Graphene and Graphene Oxide: Synthesis, Properties, and Applications," *Advanced Materials,* vol. 22, pp. 3906-3924, 2010.

[7] A. K. Geim, "Graphene: Status and Prospects," *Science,* vol. 324, pp. 1530-1534, 2009.

[8] F. Ante, D. Kälblein, T. Zaki, U. Zschieschang, K. Takimiya, M. Ikeda, *et al.*, "Contact Resistance and Megahertz Operation of Aggressively Scaled Organic Transistors," *Small,* vol. 8, pp. 73-79, 2012.

[9] J. Hedberg, "graphene transistor, 3d model of a graphene transistor," http://www.jameshedberg.com/scienceGraphics.php?sort=graphene&id=graphene-transistor-3D-model, 2013.

[10] B. Lise and R. Anderson, *Fundamentals of semiconductor devices*, C. Paulson, Ed. New York: Mc.Graw Hill, 2004.

[11] B P Luther,S P Mohney, T N Jackson, "Titanium and titanium nitride contacts to n-type gallium nitride," *Semiconductor Science and Technology,* vol. 13, pp. 1322-1327, 1998.

[12] J. A. Robinson, M. LaBella, M. Zhu, M. Hollander, R. Kasarda, Z. Hughes, *et al.*, "Contacting graphene," *Applied Physics Letters,* vol. 98, pp. 053103-053103-3, 2011.

[13] S. Russo, M. F. Craciun, M. Yamamoto, A. F. Morpurgo, and S. Tarucha, "Contact resistance in graphene-based devices," *Physica E: Low-dimensional Systems and Nanostructures,* vol. 42, pp. 677-679, 2// 2010.

[14] J. S. Moon, M. Antcliffe, H. C. Seo, D. Curtis, S. Lin, A. Schmitz, *et al.*, "Ultra-low resistance ohmic contacts in graphene field effect transistors," *Applied Physics Letters,* vol. 100, pp. 203512-1-3, 2012.

[15] D. K. Ferry, "Tunnelling," in *Quantum Mechanics*, J. Revill, Ed., ed: Taylor & Francis, 2001.

[16] J. S. Foresi and T. D. Moustakas, "Metal contacts to gallium nitride," *Applied Physics Letters,* vol. 62, pp. 2859-2861, 1993.

[17] M. Asif Khan, J. N. Kuznia, A. R. Bhattarai, and D. T. Olson, "Metal semiconductor field effect transistor based on single crystal GaN," *Applied Physics Letters,* vol. 62, pp. 1786-1787, 1993.

[18] J. D. Guo, C. I. Lin, M. S. Feng, F. M. Pan, G. C. Chi, and C. T. Lee, "A bilayer Ti/Ag ohmic contact for highly doped n-type GaN films," *Applied Physics Letters,* vol. 68, pp. 235-237, 1996.

[19] M. E. Lin, Z. Ma, F. Y. Huang, Z. F. Fan, L. H. Allen, and H. Morkoç, "Low resistance ohmic contacts on wide band-gap GaN," *Applied Physics Letters*, vol. 64, pp. 1003-1005, 1994.

[20] Z. Fan, S. N. Mohammad, W. Kim, Ö. Aktas, A. E. Botchkarev, and H. Morkoç, "Very low resistance multilayer Ohmic contact to n-GaN," *Applied Physics Letters*, vol. 68, pp. 1672-1674, 1996.

[21] B. De Jaeger, M. Van Hove, D. Wellekens, X. Kang, H. Liang, G. Mannaert, *et al.*, "Au-free CMOS-compatible AlGaN/GaN HEMT processing on 200 mm Si substrates," in *Power Semiconductor Devices and ICs (ISPSD), 2012 24th International Symposium on*, 2012, pp. 49-52.

[22] A. Fontsere, A. Perez-Tomas, V. Banu, P. Godignon, J. Millan, H. De Vleeschouwer, *et al.*, "A HfO<inf>2</inf> based 800V/300°C Au-free AlGaN/GaN-on-Si HEMT technology," in *Power Semiconductor Devices and ICs (ISPSD), 2012 24th International Symposium on*, 2012, pp. 37-40.

[23] S. Lenci, B. De Jaeger, L. Carbonell, J. Hu, G. Mannaert, D. Wellekens, *et al.*, "Au-Free AlGaN/GaN Power Diode on 8-in Si Substrate With Gated Edge Termination," *Electron Device Letters, IEEE,* vol. 34, pp. 1035-1037, 2013.

[24] Derek W. Johnson, R.T.P. Lee, Richard J. W. Hill, Man Hoi Wong, Gennadi Bersuker, Edwin L. Piner, Paul D. Kirsch, H. Rusty Harris, "Threshold Voltage Shift due to Charge Trapping in Dielectric-Gated AlGaN/GaN High Electron Mobility Transistors Examined in Au-Free Technology," *IEEE Transactions on Electron Devices,* vol. 60, pp. 3197-3203, 2013.

[25] A. Malmros, H. Blanck, and N. Rorsman, "Electrical properties, microstructure, and thermal stability of Ta-based ohmic contacts annealed at low temperature for GaN HEMTs," *Semiconductor Science and Technology,* vol. 43, p. 7, 2011.

[26] J. R. Smith, "Self-Consistent Many-Electron Theory of Electron Work Functions and Surface Potential Characteristics for Selected Metals," *Physical Review,* vol. 181, pp. 522-529, 05/10/ 1969.

[27] H. L. Skriver and N. M. Rosengaard, "Surface energy and work function of elemental metals," *Physical Review B,* vol. 46, pp. 7157-7168, 09/15/ 1992.

[28] A. K. Niessen and F. R. De Boer, "The enthalpy of formation of solid borides, carbides, nitrides, silicides and phosphides of transition and noble metals," *Journal of the Less Common Metals,* vol. 82, pp. 75-80, 11// 1981.

[29] D. K. Schroder, "Contact Resistance and Schottky Barriers," in *Semiconductor Material and Device Characterization,* ed: John Wiley & Sons, Inc., 2005, pp. 127-184.

[30] F. A. Padovani and R. Stratton, "Field and thermionic-field emission in Schottky barriers," *Solid-State Electronics,* vol. 9, pp. 695-707, 7// 1966.

[31] D. Edelstein, C. Uzoh, C. Cabral, P. DeHaven, P. Buchwalter, A. Simon, *et al.*, "A high performance liner for copper damascene interconnects," in *Interconnect Technology Conference, 2001. Proceedings of the IEEE 2001 International,* 2001, pp. 9-11.

[32] A. Hsu, H. Wang, K. Ki Kang, J. Kong, and T. Palacios, "Impact of Graphene Interface Quality on Contact Resistance and RF Device Performance," *Electron Device Letters, IEEE,* vol. 32, pp. 1008-1010, 2011.

[33] W. Li, Y. Liang, D. Yu, L. Peng, K. P. Pernstich, T. Shen, *et al.*, "Ultraviolet/ozone treatment to reduce metal-graphene contact resistance," *Applied Physics Letters,* vol. 102, pp. 183110-1-5, 2013.

[34] J. S. Moon, D. Curtis, S. Bui, M. Hu, D. K. Gaskill, J. L. Tedesco, *et al.*, "Top-Gated Epitaxial Graphene FETs on Si-Face SiC Wafers With a Peak Transconductance of 600 mS/mm," *Electron Device Letters, IEEE*, vol. 31, pp. 260-262, 2010.

[35] V. K. Nagareddy, I. P. Nikitina, D. K. Gaskill, J. L. Tedesco, R. L. Myers-Ward, C. R. Eddy, *et al.*, "High temperature measurements of metal contacts on epitaxial graphene," *Applied Physics Letters*, vol. 99, pp. 073506-1-3, 2011.

[36] A. Venugopal, L. Colombo, and E. M. Vogel, "Contact resistance in few and multilayer graphene devices," *Applied Physics Letters*, vol. 96, pp. 013512-1-3, 2010.

[37] K. Nagashio, T. Nishimura, K. Kita, and A. Toriumi, "Metal/graphene contact as a performance Killer of ultra-high mobility graphene analysis of intrinsic mobility and contact resistance," in *Electron Devices Meeting (IEDM), 2009 IEEE International*, 2009, pp. 1-4.

[38] F. P. Xia, Vasili; Lin, Yu-ming; Wu, Yanqing; Avouris, Phaedon;, "The origins and limits of metal-graphene junction resistance," *Nat Nano*, vol. 6, pp. 1748-3387, 2011.

[39] A. Kumar and C. H. Lee. (2013). *Synthesis and Biomedical Applications of Graphene: Present and Future Trends, Advances in Graphene Science*. Available: http://www.intechopen.com/books/advances-in-graphene-science/synthesis-and-biomedical-applications-of-graphene-present-and-future-trends

[40] R. Abermann, "Measurements of the intrinsic stress in thin metal films," *Vacuum*, vol. 41, pp. 1279-1282, // 1990.

[41] J. Chan, A. Venugopal, A. Pirkle, S. McDonnell, D. Hinojos, C. W. Magnuson, *et al.*, "Reducing Extrinsic Performance-Limiting Factors in Graphene Grown by Chemical Vapor Deposition," *ACS Nano*, vol. 6, pp. 3224-3229, 2012/04/24 2012.

APPENDIX

A. Procedure for the numerical solution of Poisson equation

The following steps have to followed to solve the Poisson equation in 1-D numerically

(i) Solve for the Fermi level at equilibrium for the given doping concentration. This can be done by using charge balance, viz.,

$$\int_{E_c}^{\infty} D(E)f(E).dE = N_D^+ \quad \text{(A. 1)}$$

(ii) Find the electron density at each position 'x' by assuming a voltage V(x)

$$n(x) = \int_{E_c+V(x)}^{\infty} D(E)f(E).dE \quad \text{(A. 2)}$$

(iii) Solve iteratively the above equation with Poisson equation, (2.1)

B. Transfer line method fundamentals

Figure 42(a) transfer line method (TLM) structure. It consists of two contacts of the same metal stack separated by a distance 'd' called the TLM spacing which varied across devices in the sample.

The total resistance is computed through 4-point probe measurement – a measurement technique that passes current through two probes and measures voltage across the other two probes, hence eliminating contact resistance. The advantage of using four probes instead of two is that the probe resistance is eliminated since there is no current flowing in the probes used for measuring the voltage difference in the contacts. Figure 42 (b) is called a called a TLM plot which is a plot of the total resistance for different TLM spacing. The contact resistance is extracted by extrapolating the linear plot to d=0 and

dividing the value by 2. The sheet resistance is obtained from the slope of the TLM plot. Note that 'Z' is the total width of the contact.

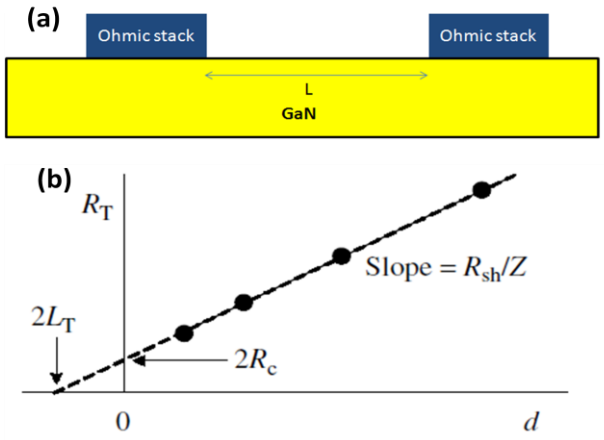

Figure 42: (a) Shows a TLM structure with the spacing L varying across the sample (b) the corresponding TLM plot , where the y-intercept gives twice the contact resistance. Reprinted with permission from [29] (Copyright [2006] by John Wiley & Sons, Inc).

There is more information, apart from contact resistance, that can be extracted be extracted from the TLM plot. This can be understood by considering the resistive network model as shown in Figure 43. The network is composed of repeated blocks of two resistances – the sheet resistance of the semiconductor, R_{sh} and the specific contact resistivity of the metal-semiconductor contact, ρ_c.

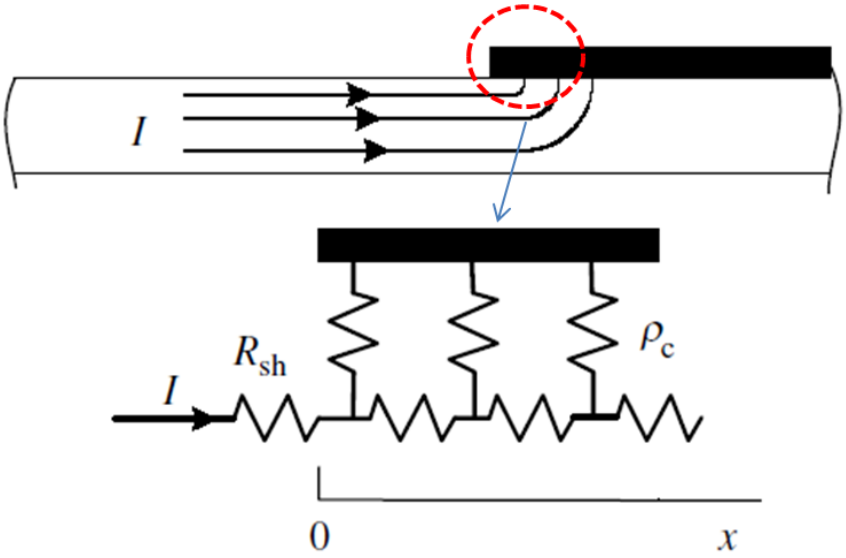

Figure 43: A resistive network model used to explain a TLM plot. Reprinted with permission from [29] (Copyright [2006] by John Wiley & Sons, Inc).

The differential equation can be described to above resistive network is given by

$$\frac{d^2V}{dx^2} = \frac{V-V_0}{L_T^2} \qquad \text{(B 1)}$$

Where V_0 is the potential of one metal pads in Figure 42(a) with respect to the other. L_T is called the transfer length and is given by the expression

$$L_T = \sqrt{\frac{\rho_c}{R_{sh}}} \qquad \text{(B 2)}$$

The solution of Eqn (B 1) takes the form $V(x) = A\exp(-\frac{x}{L_T})$ and hence the transfer length is defined as the distance into the contact at which the voltage drops by 1/e (37%) of its value at x =0. Hence we can infer that transfer length is roughly a measure of amount of current spread under the contact as shown in Figure 43.

The complete analysis of eqn (B 1) under the appropriate boundary conditions yields the result,

$$R = \frac{R_S}{Z}(L + 2L_T) \tag{B 3}$$

Hence we can that extrapolating the TLM plot to the R =0 axis, we can obtain the transfer length as shown in Figure 42(a). Once transfer length is obtained the specific contact resistivity can be calculated from eqn (B2).